



저작자표시-비영리-변경금지 2.0 대한민국

이용자는 아래의 조건을 따르는 경우에 한하여 자유롭게

- 이 저작물을 복제, 배포, 전송, 전시, 공연 및 방송할 수 있습니다.

다음과 같은 조건을 따라야 합니다:



저작자표시. 귀하는 원저작자를 표시하여야 합니다.



비영리. 귀하는 이 저작물을 영리 목적으로 이용할 수 없습니다.



변경금지. 귀하는 이 저작물을 개작, 변형 또는 가공할 수 없습니다.

- 귀하는, 이 저작물의 재이용이나 배포의 경우, 이 저작물에 적용된 이용허락조건을 명확하게 나타내어야 합니다.
- 저작권자로부터 별도의 허가를 받으면 이러한 조건들은 적용되지 않습니다.

저작권법에 따른 이용자의 권리는 위의 내용에 의하여 영향을 받지 않습니다.

이것은 [이용허락규약\(Legal Code\)](#)을 이해하기 쉽게 요약한 것입니다.

[Disclaimer](#)

Omni-directional Broadband Antireflection coating for  
solar cells using Indium Tin Oxide (ITO) based  
Fractal Structures

Sang-Hyuk Won

Department of Materials science Engineering

Graduate School of UNIST

2015

Omni-directional Broadband Antireflection coating for  
solar cells using Indium Tin Oxide (ITO) based  
Fractal Structures

Sang-Hyuk Won

Department of Materials science Engineering

Graduate School of UNIST

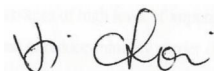
# Omni-directional Broadband Antireflection coating for solar cells using Indium Tin Oxide (ITO) based Fractal Structures

A thesis  
submitted to the Graduate School of UNIST  
in partial fulfillment of the  
requirements for the degree of  
Master of Science

Sang-Hyuk Won

7. 21. 2015

Approved by



Advisor

Kyoung-Jin Choi

# Omni-directional Broadband Antireflection coating for solar cells using Indium Tin Oxide (ITO) based Fractal Structures

Sang-Hyuk Won

This certifies that the thesis of Sang Hyuk Won is approved.

7. 21. 2015



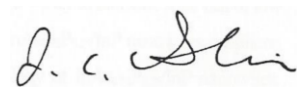
---

Advisor: Kyoung-Jin Choi



---

Thesis Committee Member #1 : Myoung Hoon Song



---

Thesis Committee Member #2 : Jae Cheol Shin



## Abstract

Solar cells have extrinsic loss from reflection of the front surface which is one such loss mechanism and has been managed in the past with the usage of planar antireflection coatings. But these coatings are each limited to a single wavelength of light and do not account for varying incident angles of the incoming light. Various nanostructures made from wet or dry etching, solution processes have shown the capability to restrict reflection for differing wavelengths and angles of incidence. Especially Graded Refractive Index nanostructures based on Indium Tin Oxide (ITO) were modeled and show a broadband, multi angled reflectance decrease due to an effective grading of the refractive index. Indium Tin Oxide (ITO) is advantageous for its ease of production, large amount, conventional process and refractive index matching to the air source region and silicon substrate.

In this study we have demonstrated Indium Tin Oxide (ITO) Fractal structures which has Graded Refractive Index (GRIN) profile for Omni-directional Broadband anti-reflection coating to silicon solar cells. Indium Tin Oxide (ITO) Graded Refractive Index Fractal structures were deposited on silicon surfaces through self-catalyst vapor liquid solid(VLS) growth mechanism using conventional Oblique Angle Deposition (OAD) with computational – controlled servo assisted electron beam evaporator while elevating substrate temperature below 200 °C. We introduced two types of silicon solar cells. The first one has polished planar surfaces and second one has pyramid structure commonly used for industrial production. Graded Refractive Index (GRIN) Fractal structures were successfully applied to planar silicon surface and exhibits both superior optical and electrical properties. With GRIN structure height 1 $\mu$ m, planar solar cell's efficiency was increased 48.9% due to reduced series resistance and reflectance while maintaining shunt resistance at normal incident angle 90°. But in the omni-directional point of view due to reduced angular reflectance up to 70° below 10%, 2 $\mu$ m GRIN structure reveals the best annual power density enhancement 73.9% compared to 68.2%. Furthermore we investigated conventional pyramid textured silicon surfaces which has self – induced oblique angle, Indium Tin Oxide (ITO) GRIN structures were deposited onto pyramid without tilting servo (normal flux incident angle 90°). The deposited GRIN 1 $\mu$ m exhibits total reflection in 300 to 1100nm wavelength length region below 5% that can enhance its annual power density 44% compared to the non-coating textured silicon solar cell. Still the surface passivation issues which is important role in crystalline silicon solar cell efficiency is remained. These issues are not discussed in this study but will be investigated further. Our results in achieving increasing annual power density using Graded refractive index anti-reflection coating is greatly encouraging as regards the development of solar cell industry.





## Contents

1. Introduction	1
1.1 solar cell operation and structures	2
1.2 Efficiency limitations and design improvements	3
1.3 Reflection minimization	3
1.4 Planar coatings	4
1.5 Textured Antireflection	6
2. Literature Review	6
2.1 Introduction	6
2.2 The physics of ARC	7
2.3 Characteristics of perfect ARC	9
2.3.1 Broadband anti-reflection	9
2.3.2 Omni – directional anti-reflection	9
2.4 Types of ARC	10
2.4.1 First generation ARC	10
2.4.2 Single layer ARC	10
2.4.3 Multiple layer ARC	10
2.4.4 Gradient refractive index ARC	11
2.5 Techniques for fabrication of Graded refractive index ARC	13
2.5.1 Sol-gel processing	13
2.5.2 Chemical vapor deposition technique	14
2.5.3 Physical vapor deposition technique	14
2.5.4 Etching	16
2.5.5 Lithography	17
3. Graded Refractive Index(GRIN) Indium Tin Oxide Anti-reflective coatings with silicon solar cells	20
3.1 Introduction	20
3.2 Experimental processes of planar silicon solar cell with GRIN nanostructures	21
3.2.1 Formation of high refractive index Nanorods	21
3.2.2 Formation of high refractive index Nanorods 3.2.2.1. Nanobranches	24
3.2.3 Graded Refractive Index (GRIN) Nanostructure formation on planar silicon	24

3.2.4	Fabrication of planar silicon solar cell with GRIN nanostructures	25
3.3	Experimental processes of planar silicon solar cell with GRIN	
	Nanostructures Graded refractive index ARC with Planar silicon solar cells	26
3.3.1	Formation of GRIN Nanostructures on micro pyramis textures silicon	27
3.3.2	Textured silicon solar cells fabrication with GRIN Nanostructures	28
3.4	Results and Discussions	29
3.4.1	GRIN ARC with planar silicon solar cells	29
3.4.1.1	XRD and TEM analysis of GRIN Nanostructures	29
3.4.1.2	SEM Images and Optical properties of GRIN Nanostructures	32
3.4.1.3	Electrical properties of planar silicon solar cells with GRIN nanostructures	47
3.4.2	ITO Nanobranched with conventional textured silicon solar cells	55
3.4.2.1	SEM images and optical properties of GRIN Nanostructures	55
3.4.2.3	Electrical properties of textured silicon solar cell with Nanobranched	58
3	Conclusions	62
4	References	63

## List of figures

Fig1. Reflection of incident light on a solar cell

Fig2. Single planar AR coating showing destructive interference of the first and second reflected waves R1 and R2 due to the quarter-wave phase difference.

Fig3. Light trapping on textured surface

Fig4. The specular reflectance of glass for light incident at angles from  $0^\circ$  to  $90^\circ$

Fig5. Comparison of the reflectance curves obtained for (a) single layer ARC (b) Double layer ARC (C) Three layer ARC,

Fig6. Smooth transition in refractive index obtained in GRIN ARC versus a sharp drop encountered in single layer ARC

Fig 7. The process steps involved in the sol-gel coating of glass using (top) spin coating and (bottom) dip coating

Fig8. Various sculpted thin films fabricated by the GLAS technique. Morphology obtained (a) with one sided oblique  $85^\circ$  flux (b) alternating oblique  $85^\circ$  flux (c) rotary substrate motion and (d) exponentially increasing flux angle.

Fig9. SEM images (a) showing a cross-sectional view of Si nanotips of length 1600 nm. (b) Cross-section of Si nanopillar arrays created by reactive ion etching through mask of PS spheres. (c) The inner structure of a chemically etched porous Si layer.[58] (d) High-density, high-aspect-ratio corkscrew-like silicon nanotips on Si substrates for reducing glare in NASA sun image sensor.

Fig 10. Schematic showing a typical nanoimprint lithography (NIL) process to replicate pattern on a thin film

Fig11. (a) A stepwise bio-replication technique using Cicadia wing as a bio-template.[119] (b) SEM image of an alumina replica of a compound eye. (c) The ommatidial array was transferred

from the original fly eye to the alumina replica. (d) An alumina replica showing the ommatidium surface with protuberances.

Fig11. Schematic illustration of Oblique angle deposition using e-beam evaporator

Fig12. Schematic illustration of High refractive index Nanorods formation

Fig 13. Self-catalyst Vapor Liquid Solid growth with Oblique Angle Deposition

Fig14. Density distribution compared to OAD and OAD-VLS

Fig15. Low refractive index nanobranched formation

Fig16. Schematic illustration of Graded Refractive Index Anti-reflection coating using Self-catalyst Vapor Liquid Solid (VLS) growth mechanism and shadow effects using Oblique angle deposition

Fig17. Process flow chart making planar silicon solar cells with GRIN nanostructures

Fig18. Optimal micro pyramid structure for industrial level of silicon solar cell

Fig 19. Self induced shadow effect in textured silicon solar cell

Fig 20. Process flow chart making conventional textured silicon solar cells

Fig 21. Schematic illustration of Self-catalyst Vapor Liquid Solid Growth mechanism

Fig 22. HR-TEM images and electron diffraction pattern of Nanostructures

Fig 23. XRD diffraction pattern of ITO thin film, Nanorods and Nanobranched

Fig24. Formation of Indium Tin Oxide (ITO) nanorods on planar silicon

Fig 25. Total reflectance spectra with varying thickness and wavelength

Fig 26. Total Solar Weighted Reflectance with varying deposition angle

Fig. 27 (a) Total reflectance and transmittance spectrum with varying Nanorods thickness, (b) Solar weighted reflectance and solar weighted transmittance with varying Nanorods thickness

Fig. 28 (a) Total reflectance and transmittance spectrum with varying deposition rates (b) Solar weighted reflectance and solar weighted transmittance with varying deposition rates

Fig. 29 (a) Haze ratio of NB 2.5  $\mu\text{m}$  without substrate rotation (b) Haze ratio of NB 2.5  $\mu\text{m}$  with substrate rotation

Fig. 30 (a) SEM images of NB 2.5  $\mu\text{m}$  without substrate rotation (b) SEM images of NB 2.5  $\mu\text{m}$  with substrate rotation

Fig 31. SEM images of nanobranched structures with varying thickness

Fig 32. Morphologies of nanobranched structures with varying thickness

Fig 33. Total transmittance and reflectance spectra with varying nanobranched structures thickness

Fig 34. Solar weighted reflectance and transmittance spectra with varying NB thickness

Fig 35. Haze ratio with varying NB thickness

Fig 36. SEM images of varying Graded refractive index fractal structures

Fig 37. Total transmittance and reflectance spectra with varying GRIN thickness

Fig 38. Solar weighted reflectance and transmittance spectra with varying NB thickness

Fig 39. Haze ratio with varying GRIN thickness

Fig 40. Variable incident angle of reflectance with varying GRIN thickness

Fig 41. Sheet resistance of  $n^+$  emitter with varying annealing temperatures

Fig 42. Dark current densities of solar cells with varying annealing temperatures

Fig 43. Ideality Factor and Saturation current densities with varying annealing temperatures

Fig 44. Solar cell top and bottom contact resistances

Fig 45. Solar cell J-V characteristics with varying thickness of GRIN nanostructures

Fig 46. Parameter enhancement factors of solar cells with varying GRIN thickness

Fig 47. Series and Shunt resistance before and after GRIN coating

Fig 48. Top and bottom contact resistance before and after GRIN annealing

Fig 49. Angular response of solar cell efficiency with respect to GRIN thickness

Fig 50. Daily maximum power density with respect to time change

Fig 51. Annual power density with respect to power density enhancement and omnidirectional enhancement

Fig 52. GRIN nanostructures on pyramid textures silicon with varying nanostructure thickness  
(a) NBs 150nm, (b) NBs 500nm, (c) NBs 1 $\mu$ m, (d) NBs 3 $\mu$ m

Fig 53. Total reflectance (a) and Solar weighted reflectance (b) with varying ITO nanobranched thickness on pyramid silicon

Fig 54. Textured silicon solar cell J-V characteristics (a) and EQE spectra (b)

Fig 55. (a) Polar plot of normalized textured silicon solar cell efficiency with varying incident light, (b) Daily integrated power enhancement with Spring/Fall, Summer, Winter at Seoul, South Korea. (c) Annual power density of pyramid and Nanobranched coated pyramid silicon solar cells

**List of tables**

Table1. Solar cell parameter characteristics

Table2 Solar cell parameters with varying GRIN thickness

Table 3. Textured silicon solar cell parameter

## 1. Introduction

Sustained attention towards energy efficiency and performance enhancements in optoelectronic devices has spurred worldwide research on ways of minimizing electrical and optical losses in devices. Fresnel reflection of light occurring in these devices is a major cause of optical loss. These losses, for instance, affect the power output from solar modules and picture quality in image sensors. Optical losses consist of light which could have generated an electron-hole pair in a device, but does not, because it is reflected from the front surface or not absorbed in the photoactive region of the device. Any change in the velocity of light, caused by two media having different refractive index, is detected as an optical disturbance, resulting in reflection of light. Silicon is used, both as an optical as well as a protective unit in many optoelectronic devices including photovoltaics (PV).

However, reflection losses in silicon amount to ~ 40% (at normal incidence) at the air-silicon interface. This loss is multiplied manifold when many transmitting optical components are involved e.g., in the case of microscope. Additionally, a reflection loss in silicon further increase as light is incident at oblique angles. That is why PV, in some cases are made to automatically track the sun throughout the day, which obviously incurs additional power consumption. Planar and textured silicon used in architectural or decorative applications, also confront aesthetic limitations due to reflection.

Fabrication of ARC on silicon has posed challenges due to stringent index matching requirements and limited choice of low-refractive index materials. For deployment of glass in outdoor conditions, such as in PV, it's also essential for the ARC to be durable and withstand exposure to various environmental conditions. Thermal mismatch and poor interfacial adhesion between ARC and substrate can raise issues of in-service delamination, thereby limiting their real time use. Similarly, adherence of dust or water droplets to a glass surface in wet or humid environments, can also affect their optical properties due to scattering of light. In this context, taking inspirations from the ways these challenges have been addressed in the natural world could offer an alternative pathway to achieving superior ARC for silicon. ARC is steadily growing, particularly on account of demand from PV, semiconductors and energy efficient infrastructures.



## 1.1 solar cell operation and Structures

Solar cells operate by absorption of photons in the solar electromagnetic spectrum in order to create electron-hole pairs, separating those charge carriers in the junction, and collection of the carriers at the terminals to drive a direct electric current [6]. Photons must be of sufficient energy to be absorbed. The energy is used to promote an electron from the valence band to the conduction band and drive the circuit. Photons of energy less than the minimum needed to excite an electron across the energy gap are reflected or transmitted by the cell. Photons of excess energy promote electrons, as well as holes, but this excess energy is lost in the form of heat due to electronic relaxation to the conduction band edge and holes to the valence band edge. Electronic conduction band promotion also creates the absence of an electron, or a hole, at the valence band. The physical interpretation of this process has the electron and hole collected at the contact terminals of the device where they enter the circuit

The most basic solar cell structure is the combination of two different types of semiconductors called a p-n junction which forms an interface through which charges interact. The different types can be made of the same original material; typically silicon is used for commercial grade cells. When the two parts are created from a single material, the n-type portion is doped with donor impurities to yield a high electron conductivity in this region. Atoms with more valence electrons than silicon (Group V elements), which has four valence electrons, are used. The p-type portion is made from doping the substance with acceptor ions, those with less valence electrons (Group III elements) than the original semiconductor. This allows for a high hole conductivity in this region [3]. The dopants create a junction with a built-in potential, eliminate the need for a bias voltage, and adjust the valence and conduction band energy levels. This asymmetry is the basic requirement for photovoltaic energy conversion in a solar cell [6]. The Fermi energy, the energy at which the probability of electron occupation is exactly one-half, is split into two quasi-Fermi levels, one for electrons and one for holes. This describes the illuminated state of the cell. The difference between the quasi-Fermi energies corresponds approximately to the output voltage, while the output current can be calculated from the number of absorbed photons and their quantum efficiency [6]. The charge carrier separation occurs in the depletion region, with typical width  $\sim 1$  micrometer while the absorption process extends over the whole thickness of 200 micrometer. This absorber layer is approximately 150 to 250 microns thick [7]. This is a large amount of material and contributes significantly to the cost of modules.

### 1.2 Efficiency Limitations and Design improvements

Design improvements create better functioning solar power devices. There are two types of limitations which adversely affect solar cells, intrinsic and extrinsic limitations. Photovoltaic devices can be improved in a few select ways in order to overcome their extrinsic limitations. The intrinsic limitations cannot be overcome by design. They include incoming light energy limitations due to the range of the solar spectrum, Auger recombination, free carrier absorption, and radiative recombination [8, 9]. Extrinsic limitations can be overcome and include surface recombination, contact shadowing, series resistance, incomplete collection of photo-generated carriers, and reflection at the front surface, among others [10]. While all of these are important, without allowing the light to enter the cell, none of the other extrinsic limitations factor into cell performance. Therefore, reflection at the front surface is the first and most basic problem to overcome in cell design.

### 1.3 Reflection Minimization

The design of efficient photovoltaic devices requires the limiting, or eliminating, of power conversion loss mechanisms, including reflection of incoming light, at the front surface. Reflection occurs when light travels from a medium to another medium with differing index of refraction. For a solar cell, three different types of incident radiation reflection occur including reflections from contacts, back surfaces, and front surfaces as seen in figure 1.2. The topic of this thesis will focus on front surface reflection minimization

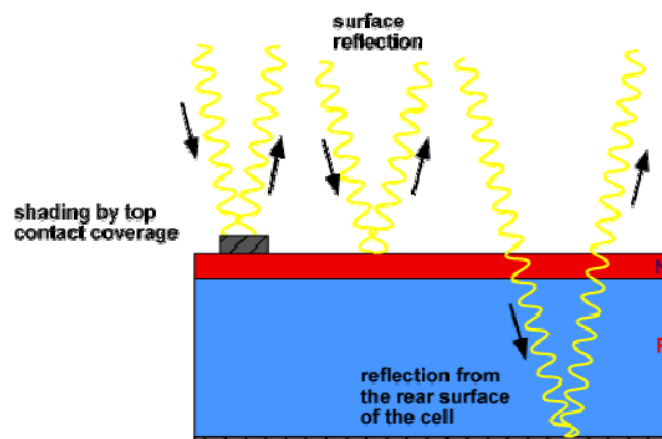


Fig1. Reflection of incident light on a solar cell

The methods employed to limit reflectivity in solar cells are texturing of the surface and applying planar antireflective coatings. Texturing is used to increase scattering into the cell, which increases the

probability of capturing a photon from the incident light, and light trapping which lengthens the path length and increases the probability of electronhole pair production from photon absorption. Planar coatings produce destructive interference with reflected waves and decrease the refractive index of the medium on which the light is incident. The employment of antireflective coatings has greatly diminished this problem [12]. By using a thickness equal to one-quarter times the incident wavelength, reflections can be minimized. However, these coatings are for a single wavelength and must be applied in successive layers for broadband effects. The planar coatings do not take into account the different angles at which light can be incident [13]. Successive layering of individually antireflective coatings will aid performance of a cell but also increases manufacturing costs and difficulty.

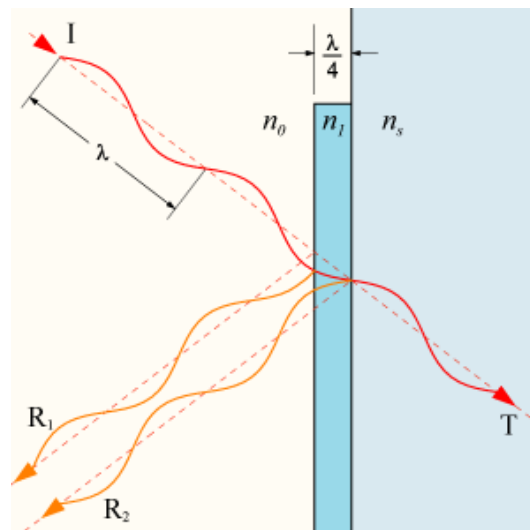


Fig2. Single planar AR coating showing destructive interference of the first and second reflected waves R<sub>1</sub> and R<sub>2</sub> due to the quarter-wave phase difference.

#### 1.4 Planar Coatings

Planar anti-reflection coatings are deposited at a depth of one-quarter of the wavelength of incoming light. For each wavelength, there must be an additional coating to minimize reflection. Since this is not possible in practice, a few different planar surfaces are used to minimize reflection at the wavelengths associated with maximum intensity in the incident spectrum. From the Fresnel equation for reflectivity, the ideal index of refraction is for an anti-reflection coating can be found. At normal incidence, with a single AR coating of index  $n_1$ , the Fresnel equation, from the field boundary

conditions for three media with indices of refraction for the incident and substrate media  $n_0$  and  $n_2$ , takes the form

$$R = \left| \frac{(r_{01} + r_{12})^2 - 4r_{01}r_{12} \sin^2\left(\frac{2\pi d}{\lambda}\right)}{(1 + r_{01}r_{12})^2 - 4r_{01}r_{12} \sin^2\left(\frac{2\pi d}{\lambda}\right)} \right|^2$$

Where  $d$  is the AR layer thickness,  $\lambda$  is the incident wavelength, and  $r_{01}$  and  $r_{12}$  are:

$$r_{01} = \frac{n_0 - n_1}{n_0 + n_1} \text{ and } r_{12} = \frac{n_1 - n_2}{n_1 + n_2}$$

With a thickness of a quarter-wavelength, the sine function terms in the numerator and denominator are zero

$$\sin^2\left(\frac{2\pi}{\lambda}d\right) = \sin^2\left(\frac{2\pi}{\lambda} * \frac{\lambda}{4}\right) = \sin^2\left(\frac{\pi}{2}\right) = 0$$

The reflection equation is minimized when  $R = 0$  and is now:

$$\begin{aligned} R &= \left| \frac{(r_{01} + r_{12})^2}{(1 + r_{01}r_{12})^2} \right|^2 = \left| \frac{\frac{n_0 - n_1}{n_0 + n_1} + \frac{n_1 - n_2}{n_1 + n_2}}{1 + \left(\frac{n_0 - n_1}{n_0 + n_1}\right)\left(\frac{n_1 - n_2}{n_1 + n_2}\right)} \right|^2 \\ &= \left| \frac{\frac{(2n_0n_1 - 2n_1^2)}{(n_0 + n_1)(n_1 + n_2)}}{\frac{(n_0 + n_1)(n_1 + n_2) + (n_0 - n_1)(n_1 - n_2)}{(n_0 + n_1)(n_1 + n_2)}} \right|^2 \\ &= \left| \frac{(2n_0n_1 - 2n_1^2)}{(n_0 + n_1)(n_1 + n_2) + (n_0 - n_1)(n_1 - n_2)} \right|^2 = 0 \end{aligned}$$

Which yields

$$n_{AR} = n_1 = \sqrt{n_0n_2}$$

Therefore, to minimize reflection from a planar surface, it must be coated with a coating of thickness equal to one-quarter the size of the incident wavelength and have an index of refraction equal to the geometric mean of the media which it separates.

### 1.5 Textured Antireflection

An omni-directional, antireflection scheme is desirable to cover a broadband of the electromagnetic spectrum for varying angles of incidence. This can be achieved with texturing of the surfaces. Texturing changes the entrance angle as light enters the cell and extends the optical path length which allows for increased chances of absorption (figure 1.4). This can also be achieved by deposition of tapered nanostructures onto cells. Since these structures can be readily deposited from low-cost materials and utilizing simple technology, nanostructures are considered cost-effective and results-enhancing ways to maximize the efficiency of solar cells [15].

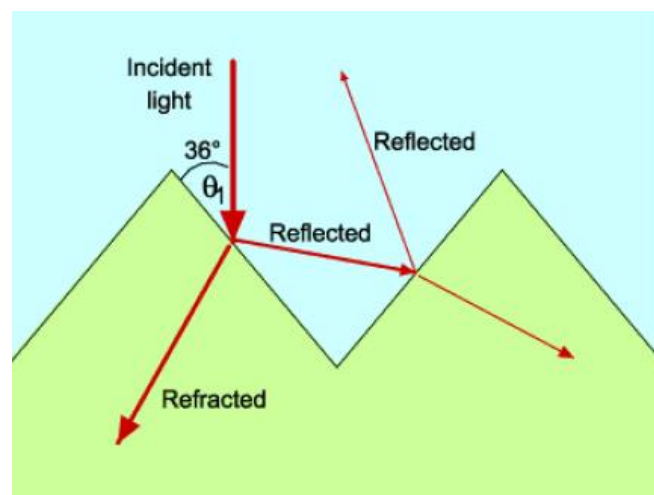


Fig3. Light trapping on textured surface

## 2. Literature Review

### 2.1 introduction

Light transmission and production has been an area of profound interest in physical sciences. The explanation of structural color of silverfish and peacock offered by scientists modified the popular notion of coloration.[27] Interaction of light with different structures became an area of active research and optical phenomena such as interference and scattering of light explained the rich diversity of colors seen in biological species. It was this quest for understanding nature's optical strategy that laid the

foundation of anti-reflectivity. The large lusterless eyes of nocturnal moths were analyzed for the first time using ultra-powerful scanning electron microscopes. The cuticular protuberances called nipple arrays on the cornea of the moths were found to be an effective biomimetic pathway to achieving superior anti-reflectivity.[23,24] The concept of anti-reflectivity was initially proposed by Lord Rayleigh in the 19th century based on a serendipitous observation of tarnishing of glass improving its transmittance than lowering it.[28] This led to the idea of achieving anti-reflectivity by incorporating a thin-film at an interface (e.g., substrate/air) with a relatively lower refractive index than that of the substrate. The first antireflective coatings (ARC) on glass were fabricated in 1817 by Fraunhofer based on his observation that reflection was reduced as a result of etching a surface in an atmosphere of sulphur and nitric acid vapor.[29] Over the years ARC have been studied in great detail and numerous nanofabrication techniques have been explored for their fabrication. ARC have also been commercially used in an exceedingly large-number of optoelectronic devices such as surface-emitting lasers, optical data storage, camera lenses eyeglasses, sensors for aeronautical applications, automotive glass, flat panel displays etc.[2,3,30-33] ARC on top glass cover of photovoltaics (PV) have helped reduce reflectance of the PV over a broad spectrum and oblique angles of incidence. As for solar cells, silicon nitride or titanium dioxide coatings of submicron thickness have produced effective reduction in reflectance.[8,34] Textured front surface of solar cells especially in mono-crystalline silicon has also helped increase light coupled to the cell thereby maximizing its efficiency.[35]

## 2.2 The physics of ARC

Reflection is caused when light encounters an abrupt change in medium during its propagation. A medium (glass, water, air, etc.) is characterized optically by the parameter, refractive index ( $n$ ) which quantifies the speed of light in the current medium with respect to that in vacuum. Thus, as light travels, eyes can spot an optical disturbance in the form of reflection if there is a change in refractive index. According to Fresnel, the fraction of incident light reflected at the interface is measured by reflectance,  $R$  and the rest transmitted (refracted) is measured by transmittance,  $T$ .

The following assumptions are made to formulate the conditions for antireflection:

1. The reflected waves have the same intensity.
2. Other optical interactions such as scattering, absorption, etc., are negligible.

The expression for reflection for light propagating through a single layer thin-film

(shown in Figure 2.1 (a)) is given by the following relationship: [36]

$$\begin{bmatrix} B \\ C \end{bmatrix} = \begin{bmatrix} \cos \delta_1 & \frac{(i \sin \delta_1)}{\eta_1} \\ i\eta_1 \sin \delta_1 & \cos \delta_1 \end{bmatrix} \begin{bmatrix} 1 \\ \eta_0 \end{bmatrix} \quad (2.1)$$

$$Y = \frac{C}{B} \quad (2.2)$$

$$R = \left( \frac{\eta_0 - Y}{\eta_0 + Y} \right) \left( \frac{\eta_0 - Y}{\eta_0 + Y} \right)^* \quad (2.3)$$

Here,  $\eta_1$  has two different expressions for the two different polarization states of light (namely, s and p). For p-polarized light,  $\eta_r = nr / \cos \theta_r$  and for s-polarized light,  $\eta_r = nr \cos \theta_r$ .

Applying Snell's law to the following case we get:

$$\eta_0 \sin \theta_0 = \eta_1 \sin \theta_1 = \eta_2 \sin \theta_2$$

The criterion for achieving perfect anti-reflectivity is that all the reflected waves undergo destructive interference and  $R = 0$ . Applying the condition for destructive interference, we get  $\delta = k\pi/2$ , which implies that the reflected waves are  $\pi$  radian out of phase. Considering normal incidence, that is  $\theta_r = 0$ , we get

$$d_1 = \frac{\lambda}{4n_1}$$

This implies that the thickness,  $d_1$  of the anti-reflective coating (single-layer) must be sub-wavelength. Assuming normal incidence and substituting (2) and (3) in equation (1) we get

$$R = \left[ \frac{n_0 n_2 - n_1^2}{n_0 n_2 + n_1^2} \right]^2$$

Applying the condition  $R = 0$ , we get,  $n_1 = \sqrt{n_0 n_2}$ . This implies that the refractive index of the ARC must be geometric mean of the indices of the substrate and the surrounding medium. In summary, the two conditions for single-layer ARC on a substrate are the following

- Thickness of the coating =  $\lambda/(4 n_1)$ .
- Refractive Index,  $n_1 = \sqrt{n_0 n_2}$ .

## 2.3 Characteristic of perfect ARC

### 2.3.1 Broadband anti-reflection

Suppression of Fresnel reflection in a substrate (e.g., glass) over a broad range of wavelengths of the incident light is called broadband anti-reflection.[3] Design of ARC based on refractive index matching in the visible region of incident light, doesn't ensure a match in the ultraviolet (UV) or the near infrared (NIR) region. This affects the transmittance of ARC glass for wavelength other than the target region. However, broadband ARC that can suppress reflection over a wider spectrum of incident light are highly desirable in various optoelectronic devices. Current research in broadband ARC is mostly centered on multiple layer ARC and gradient refractive index coatings.

### 2.3.2 Omni-directional anti-reflection

The reflection of light, in both forms of polarization, increases in direct proportionality with the angle of incidence beyond a critical angle called the Brewster's Angle (Figure 2.4). Many optoelectronic devices, PV for instance, experience large variations in solar incident angles annually, which may introduce inconsistency in their performance.[44] Secondly, eyeglasses with ARC often appear reddish when looked at an angle. This is due to higher reflections observed at increasingly oblique angles of incidence. Thus, ARC for glass, Si or other substrates have to be designed to offer consistent reduction in reflection over a wider range of incident angles. Strategies to achieving such superior antireflective property involve replicating nanostructures found in the eyes of moths or vacuum depositing materials of gradually reducing refractive index.[35]



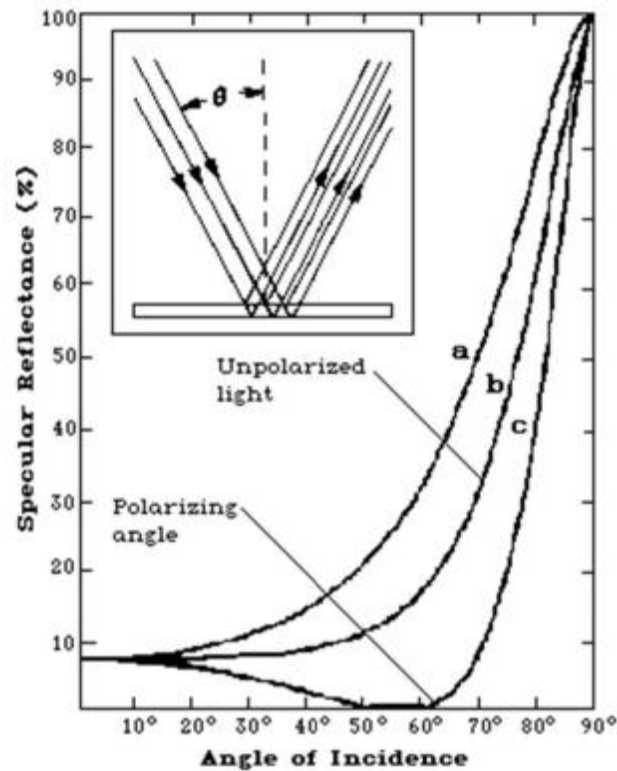


Fig4. The specular reflectance of glass for light incident at angles from 0 to 90

## 2.4. Types of ARC

### 2.4.1 First generation ARC

1. Single layer ARC : The objective of a single layer ARC was to achieve destructive interference of incident light by creating an optical path difference of  $\lambda/2$ , or an odd multiple  $\lambda/2$ . [1] Single layer ARC were found to moderately suppress reflectance at the target wavelength, for which they are designed (Figure 2.5(a)). In case of Si solar cells, materials suitable for single-layer ARC such as  $\text{TiO}_2$ ,  $\text{SiN}_x$ ,  $\text{ZnO}$  etc. have been studied for reducing reflectance and enhancing their efficiency. [8,34,47] However, in the case of glass the calculated ideal refractive index of typical single-layer ARC is 1.22. Finding a suitable material with such lower refractive index for application as ARC on glass is a challenge

### 2.4.2 Multiple layer ARC

Multiple layer ARC are designed to offer

Reflectance suppression over a broader spectrum than single layer ARC. Doublelayer or bilayer ARC

for instance, can achieve zero reflectance with equal optical thickness ( $n_1d_1 = n_2d_2 = \lambda/4$ ), if a high index layer (such as aluminum oxide with refractive index 1.69) is coated prior to the low-index layer (such as magnesium fluoride with refractive index 1.38). The reflectance of double-layer ARC resembles a V-shape, as shown in Figure 2.5(b) which is why they are alternatively called V-coatings. Reduction in reflection over a much broader spectrum was achieved by realizing triple layer ARC on substrates. Figure 2.5(c) shows the reflectance profiles of triple layer ARC on glass obtained by stacking a sub-wavelength thin-film of magnesium fluoride on a film of zirconium dioxide followed by a sub-wavelength film of cerium (III) fluoride on glass. Similarly, an example of multi-layer ARC is the SiO<sub>2</sub>/SiO<sub>2</sub>-TiO<sub>2</sub>/TiO<sub>2</sub> triple-layer ARC fabricated on monocrystalline Si solar cells that reduced the reflectance of Si up to 3.2%. [49] Multiple layer ARC are designed to achieve a gradient refractive index, which is discussed in the next section.

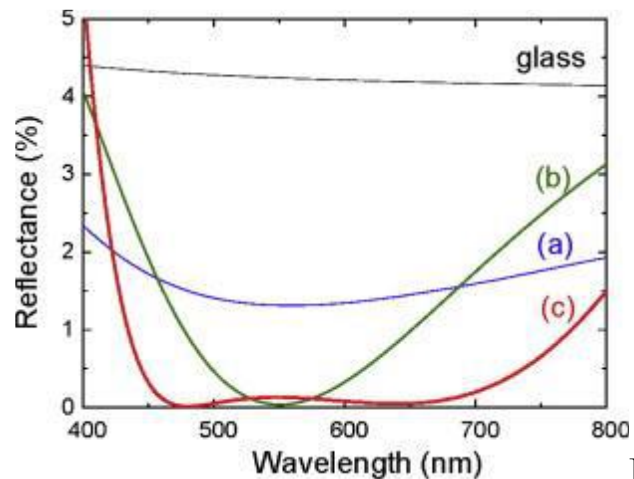


Fig5. Comparison of the reflectance curves obtained for (a) single layer ARC (b) Double layer ARC (C) Three layer ARC

#### 2.4.3 Gradient refractive index ARC

Gradient refractive index (GRIN) ARC were designed to achieve both broadband and omnidirectional anti-reflective property. [49-52] As shown in Figure 2.6(a) and Figure 2.9(a), a gradual transition in refractive index from air to substrate presents a scenario, theoretically explained by Lord Rayleigh to produce much less reflection than an abrupt media. [28] Additionally, gradient index optics takes advantage of the gradual inward bending of light incident at oblique angles (Figure 2.9 (a)). Thus, as light rays deviate less from the normal, their transmittance naturally increases through the substrate thereby, enhancing the omnidirectional anti-reflective property. [52] The refractive index profiles of

the GRIN ARC follow certain mathematical expressions such as linear, parabolic, cubic or higher order functions. Southwell has proposed the following equations defining various gradient refractive index (GRIN) profiles

- Linear index profile,  $n = n_i + (n_s - n_i) t$ ,  $0 \leq t \leq 1$  (2.9)

- Cubic index profile,  $n = n_i + (n_s - n_i) (3t^2 - 2t^3)$  (2.10)

- Quintic index profile,  $n = n_i + (n_s - n_i) t (10t^3 - 15t^4 + 6t^5)$  (2.11)

Where,  $n_i$  and  $n_s$  are the refractive index of the incident medium and substrate respectively and  $t$  is the thickness of the film. Southwell showed that such sequences of polynomials, describing a graded interface do not indefinitely enhance the anti-reflective property. Based on his analysis, quintic index profiles of thickness close to the wavelength of light behave as near optimum GRIN ARC.[53] In 2007, Xi et al. experimentally verified this hypothesis by fabricating GRIN ARC comprising TiO<sub>2</sub> and SiO<sub>2</sub> nanorods inclined at different angles.[54] They observed that these unique structures reduced the reflectance of Si substrates, to values  $< 0.1\%$ , regardless of the polarization of light (Figure 2.6 (b)). They also fabricated a hybrid multi-layer configuration having three layers of TiO<sub>2</sub> nanorods and two layers of SiO<sub>2</sub> nanorods above it, on Si substrates, as shown in Figure 2.6 (c). A gradual transition in refractive index from 2.03 at the bottom to 1.05 at the top produced a reduction in reflectance of  $\sim 0.3\%$  for incident angles from  $0^\circ$  to  $55^\circ$ . One of the limitations of the GRIN ARC is the difficulty in finding materials with refractive index suitable for various other substrates, such as glass. While such suitable low refractive index materials may not be directly available in nature creating them often involves complicated and expensive fabrication processes. Additionally, materials comprising the subsequent layers should have very good bonding between layers as well as with the substrate. Substrates equipped with ARC are often exposed to outdoor conditions and any delamination within the layers, caused by thermal effects or mechanical stress, might also deteriorate the performance of the ARC thereby limiting their durability.

F

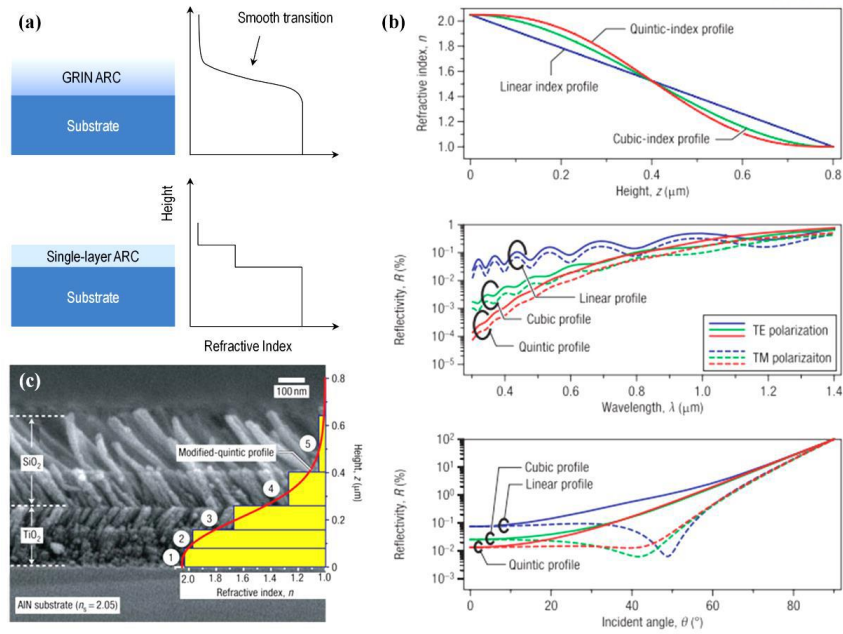


Fig 6. Smooth transition in refractive index obtained in GRIN ARC versus a sharp drop encountered in single-layer ARC. (b) Shapes of linear, cubic and quintic refractive index profiles with respect to the height of ARC, calculated reflectance of these profiles for different wavelengths of visible light and different incident angles. (c) Cross-sectional SEM image of a GRIN ARC with a quintic-index profile. The gradient index coating consists of three layers of  $\text{TiO}_2$  nanorods and two layers of  $\text{SiO}_2$  nanorods

## 2.5 Techniques for fabrication of ARC

### 2.5.1 Sol-gel processing.

The most commonly used techniques for sol-gel synthesis of ARC are dip-coating and spin-coating. In dip coating (illustrated in Figure 2.10 (top)) the substrate is immersed into a precursor solution (sol-gel) and withdrawn at a controlled speed. On the other hand, spin-coating (illustrated in Figure 2.10 (bottom)) involves rotation of the substrate with a precursor dispersed on its surface, at a controlled speed. The precursor is prepared by mixing metal organic compound in an organic solvent. The solution is either dip- or spin-coated on the substrate, followed by gelation during the evaporation of the solvent. A final heat treatment of the coated film transforms it into metal oxide or fluoride (depending on the precursor incorporated) and leads to removal of the organic byproducts present in the film. Sol-gel processing has been in use for commercial scale production of ARC glass since 1964. The foremost ARC manufactured for commercial purpose were multi-layer ARC such as a three-layer  $\text{TiO}_2/\text{SiO}_2\text{-TiO}_2$ -

SiO<sub>2</sub> ARC on silicate glass with applications such as framing glass for paintings, plastic lenses, architectural glass and detachable contrast enhancement filters for monitors.[49]

Porous ARC have also been fabricated by the sol-gel technique. One particularly notable approach involving sol-gel technique, was developed by Walheim et al. to fabricate porous polymer ARC. This approach involved phase-separation of a binary polymer blend such as, polystyrene and polymethyl-methacrylate (PMMA) in tetra-hydrofuran (THF), during spin coating. This was followed by selective dissolution of one of the polymers by using a suitable solvent, such as cyclohexane in the above case. The desired minimum pore-size and maximum pore-volume was achieved by varying the mixing ratio in the mixture of two insoluble materials judiciously. The authors noted that if the length scales of the pores are much below visible wavelengths, a transmittance of 99.7% is obtained between 400.600 nm.

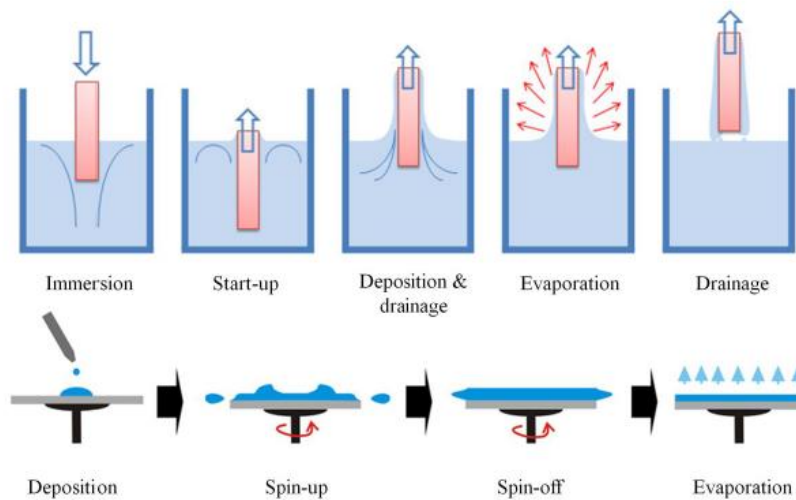


Figure 7. The process steps involved in the sol-gel coating of glass using (top) spin coating and (bottom) dip coating

### 2.5.2 Vapor deposition techniques

Vapor deposition has been the most widely used commercial technique for the fabrication of ARC.[1] Plasma enhanced chemical vapor deposition (PECVD), for instance, is commonly employed to produce nitride-based ARC such as Silicon nitride (SiN<sub>x</sub>:H) coatings on textured Si solar cells. The nitride coatings function both as ARC and surface passivation layer for Si solar cells.[8] The deposition technique involves reaction e.g., between silane and ammonia and deposition of the volatile precursor(s) on a heated substrate. Development in plasma assisted evaporation processes has also enabled deposition of ARC on glass, GaN and polymer substrates. Industries, worldwide have explored various

evaporation techniques for development of multi-layer hybrid coatings comprising antireflective layers atop scratch-resistant layers.

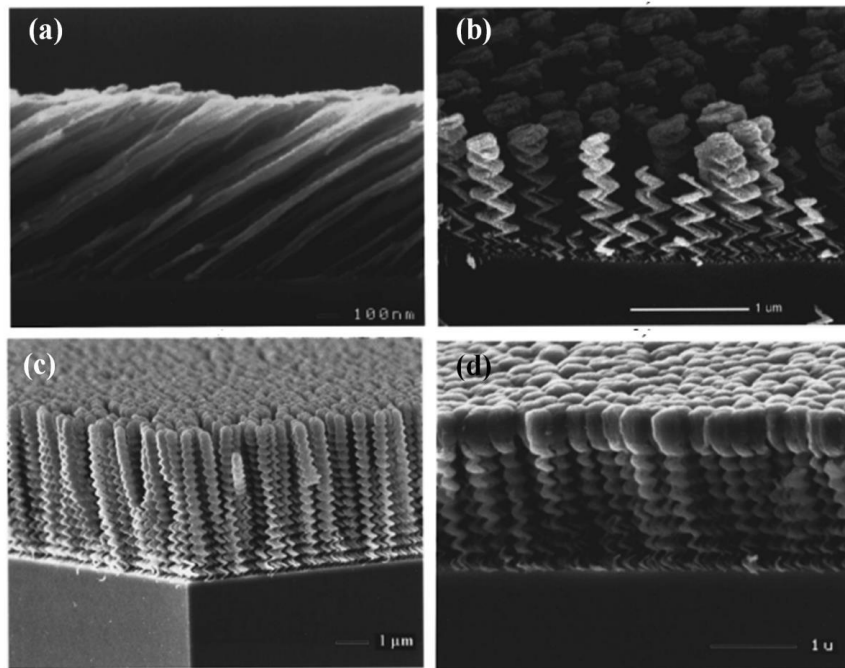


Figure 8. Various sculpted thin films fabricated by the GLAS technique. Morphology obtained (a) with one sided oblique  $85^\circ$  flux (b) alternating oblique  $85^\circ$  flux (c) rotary substrate motion and (d) exponentially increasing flux angle.

Vapor deposition has also been applied to the fabrication of GRIN ARC on Si by a new fabrication technique called glancing angle deposition (GLAD). In this technique, vapor flux, incident at an angle, is deposited on a rotating substrate. This allows the thin film to grow with a gradually decreasing density or increasing porosity. The porosity of the film is dependent on the angle of vapor incidence. It was observed that if the material was deposited at large oblique angles, the porosity of the film increased in higher proportions and vice versa. Structures with unusual morphologies called sculptured thin film (STF) were fabricated by this technique. Films with slanted, chevron, helix, vertical and other morphologies (Figure 2.11 (a)–(d)) led to achieving different refractive index profiles. For example, structures made of  $\text{SiO}_2$  exhibited a Gaussian profile refractive index with highest transmittance of 99.9% (up to 460 nm).

### 2.5.3 Etching

Etching has been used for the fabrication of anti-reflective nanostructures such as moth's eye nanostructures or sub-wavelength structure arrays on various substrates as shown in Figure 2.12. This process has commonly relied on the use of a mask or an arrangement of particles that mimics a mask.[32,35,99-104] For example, a monolayer of self-assembled spheres such as silica colloidal crystals served as a mask for etching Si substrates for fabrication of ARC. Sun et al. incorporated the above mask on Si substrates and performed a SF<sub>6</sub> dry etching to fabricate moth's eye nanostructures on the substrates.[109] The diameter and height of the nanostructures were determined by the size of spheres and etching time. They reported a reduction in reflectance of 2.5% for Si substrates. Similarly, Si nanotips by plasma etching using reactive gases comprising silane (SiH<sub>4</sub>), methane (CH<sub>4</sub>), hydrogen (H<sub>2</sub>) and argon (Ar) (Figure 2.13(a)), pyramidal structures fabricated by etching Si, covered with monolayer of polystyrene spheres as mask (Figure 2.12(b)), sub-wavelength structures by using porous alumina membrane as mask and high aspect ratio corkscrew-like silicon nanotips by using a polymer grass mask (Figure 2.12(d)) are examples of various

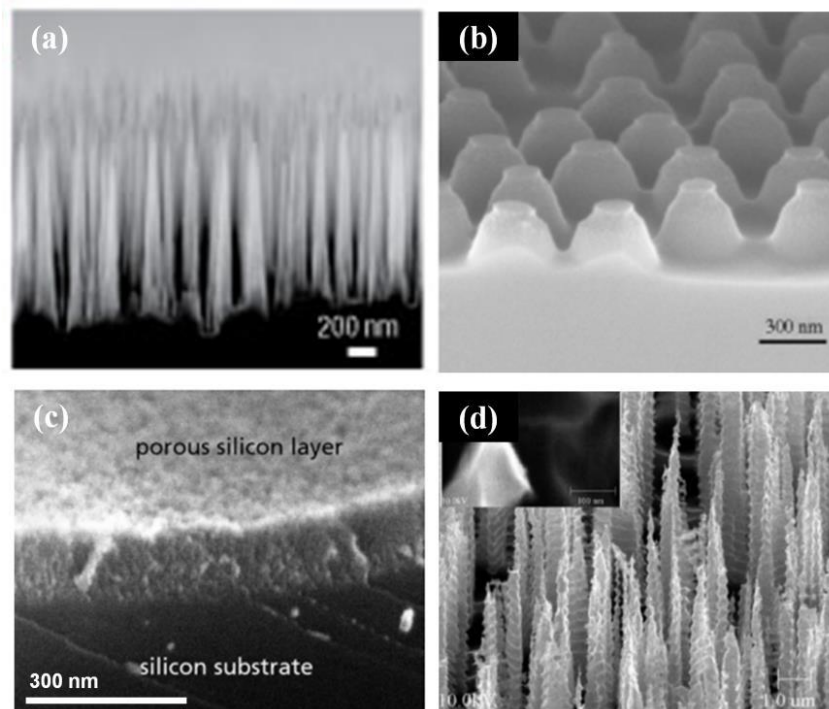


Fig9. SEM images (a) showing a cross-sectional view of Si nanotips of length 1600 nm. (b) Cross-section of Si nanopillar arrays created by reactive ion etching through mask of PS spheres. (c) The inner structure of a chemically etched porous Si layer. (d) High-density, high-aspect-ratio corkscrew-like silicon nanotips on Si substrates for reducing glare in NASA sun image sensor.

Wet etching approaches have also been developed for fabricating porous SiO<sub>2</sub> ARC on glass, notably by Liu et al.

#### 2.6.4 Lithography

The discovery of anti-reflective nanostructures in the compound eyes of moths spurred the interest of scientists to develop synthetic replicas of the nanostructure arrays. Their efforts were sustained in large part by development of lithography based patterning which had already made significant inroads into the semiconductor industry. Clapham et al. were the first to use interference lithography to fabricate moth's eye anti-reflective nanostructures on glass. They utilized the fringe patterns produced by the interference of two laser beams aligned to each other at 120°. A photoresist exposed to the interference pattern after development (chemical treatment), produced sinusoidal protuberances that resembled the moth's eye antireflective nanostructures. However, they found that the technique allowed only limited control over height of the nanostructures which is a crucial factor in achieving effective anti-reflection property. This was because the height of the arrays depended on the duration of exposure and photoresists being sensitive to shorter wavelengths, could not be exposed for a longer time period.

A high resolution technique called Electron-beam lithography (e-beam lithography) solved the issues of overexposure and provided better control over the height of the nanostructures. Arrays of anti-reflective nanostructure comprising a suitable photoresist were fabricated using e-beam lithography and were transferred to substrates such as Si or glass by etching. Kanamori et al. proposed an e-beam lithography followed by SF<sub>6</sub> fast atom beam etching (FAB) to produce conical anti-reflective nanostructure arrays on Si substrates. After the desired nanostructure patterns were fabricated in the resist layer, the patterns were transferred into Si substrate by an etching process. A periodicity of 150 nm and structure height of 350 nm could be achieved and a broadband reduction in reflectance of less than 3% was reported by the group. Toyota et. al. demonstrated that e-beam lithography along with a



chrome mask-assisted reactive ion etching can fabricate moth's eye nanostructures in fused silica. The reflectance of the fused silica substrate was reported to be less than 0.5% for wavelengths from 400 – 800 nm. However, the e-beam writing on an area as small as 1.2 mm × 1.2 mm took about 10 h to complete. A pattern transfer technique called Nanoimprint lithography (NIL), developed in 1996 received great attention due to its simplicity and has since made significant progress in high throughput patterning with great precision. It has also proved to be an economical process. In 2003, the International Technology Roadmap for Semiconductors (ITRS), recognized NIL as one of the candidates for future integrated circuit production.

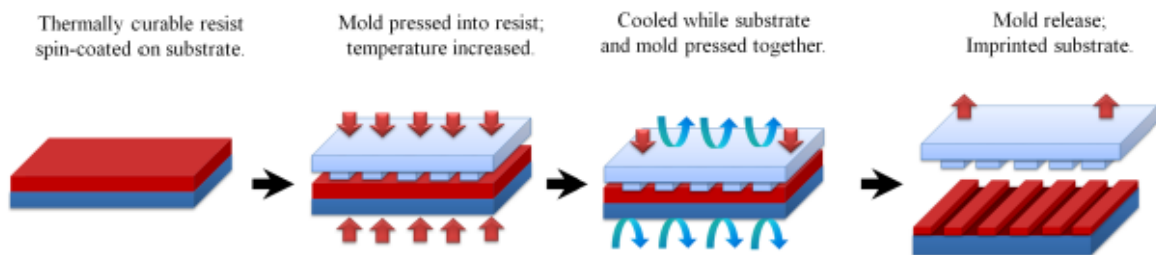


Fig 10. Schematic showing a typical nanoimprint lithography (NIL) process to replicate pattern on a thin film

Figure 10 shows a schematic of the process steps involved in the NIL fabrication technique. A master mold containing nanoscale-relief features, is embossed onto a resist (polymer based) thin-film formed on a substrate. The embossing is carried out at a controlled pressure and temperature to ensure conformal filling of the resist within the crevices of the patterns. Temperature plays a crucial role in cross-linking of the resist as well as effective curing or hardening of the resist thereby preserving the imprinted pattern. Since NIL depends on mechanical deformation of the resist materials, it can achieve structural resolutions beyond the limitation set by diffraction of light or scattering of beams – issues that are encountered in other lithography techniques. A variation of the NIL technique called ultra-violet (UV) NIL, uses UV-curable resists and a transparent stamp for imprinting. Instead of thermal curing, UV exposure cures the resist during imprinting. To accurately reproduce the biological anti-reflective nanostructures many researchers have directly used the natural sources as template for replication. Xie et al., for instance, demonstrated that the wings of Cicadia's (*Cryptympana atrata* Fabricius) can be used as a bio-template to replicate the anti-reflective nanostructures on its wings, as shown in Figure 2.14(a). The wings of cicadia served as molds for directly imprinting the nanostructure patterns into a PMMA thin-film. To avoid any surface damage to the cicadia wings, most recently Zhang et al. have demonstrated the use of photocurable liquid perfluoropolyether (PFPE) that lowers the surface energy of

the mold to facilitate

easy release after replication. In fact, some scientist have also replicated the multi-scale, ommatidia (convex micro-lens arrays) with anti-reflective nanostructures, found in the compound eye of certain arthropods, using the same approach. Huang et al. have reported a technique comprising atomic layer deposition of alumina ( $\text{Al}_2\text{O}_3$ ) precursor followed by curing of the same at  $500^\circ\text{C}$ , to produce  $\text{Al}_2\text{O}_3$  molds of a fly's compound eye, as shown in Figure 2.14(b)-(d).

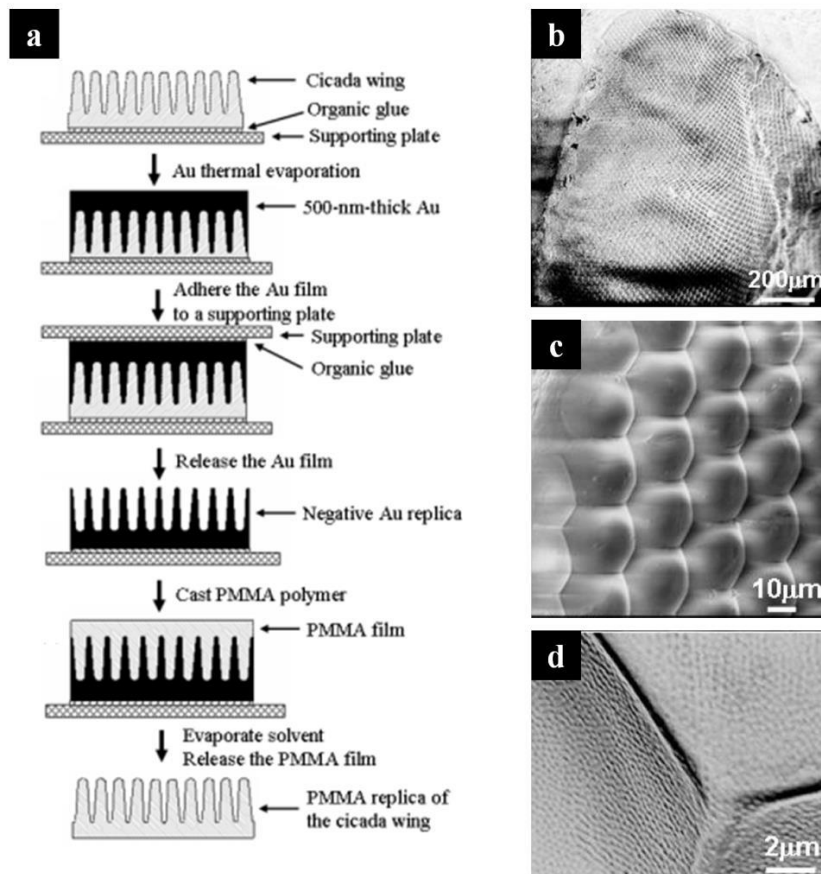


Fig11. (a) A stepwise bio-replication technique using Cicadia wing as a bio-temple. (b) SEM image of an alumina replica of a compound eye. (c) The ommatidial array was transferred from the original fly eye to the alumina replica. (d) An alumina replica showing the ommatidium surface with protuberances.

A minimum reflectance of 0.7% for Si substrate, that only increased to a marginal 0.96% at an incident angle of  $80^\circ$ , showed great potential for obtaining omnidirectional anti-reflective property. The original fly eye was, however, lost during the annealing. Ko et al. have demonstrated a similar strategy to replicate ommatidial morphology found in *Attacus atlas* moth. They have

demonstrated the use of photocurable liquid perfluoropolyether (PFPE) for efficient pattern transfer from the insect's compound eyes. Master molds have also been made by e-beam lithography or other techniques and have been made commercially available by NIL Technology, Ltd. etc.

Moth eye nanostructures have been fabricated by NIL on substrates ranging from glass to solar cells. NIP-K28™ imprinted glass substrates with a transmittance of 95%, polyvinyl chloride (PVC) imprinted moth's eye nanostructure arrays (transmittance, 96%) and PMMA moth's eye nanostructures enhancing transmittance to 96% are some of the relevant examples. UV-curable resin (NIP-K28™) based anti-reflective nanostructures on commercial GaAs solar cell, PMMA moth's eye layers on polycrystalline Si solar cells and most recently, AlInP nanostructures on dilute nitride solar cells have also led to appreciable improvement in the efficiency of solar cells.

### 3. Graded Refractive Index (GRIN) Indium Tin Oxide Anti-reflective coatings with Silicon solar cells

#### 3.1 Introduction

Anti-reflection property can be imparted to a substrate by fabrication of a thin film of sub-wavelength thickness ( $\lambda/4$ ) on the substrate. The refractive index of the thin-film must be matched to the geometric mean of the refractive indices of the substrate and the ambient medium. The above preconditions enable destructive interference of reflected light rays at the interface, thereby minimizing Fresnel reflections. For materials point of view there are many materials which fits to conventional antireflection coatings for silicon solar cell. However among the available materials to silicon solar cell, only few materials are used for ARC coating such as refractive index 2 for Titanium dioxide, 1.4 for Silicon dioxide, 1.23 for Magnesium Fluoride, 1.9 for Indium Tin oxide (ITO). Also There has been suffered from lack of extremely low refractive index materials under 1.5. Especially, the Indium Tin Oxide (ITO) has its both novel electrical and optical properties. In addition ITO is broadly adopted to recent industry for fabrications of devices (i.e Light Emitting Diode, Solar cells). To make Graded refractive index structures, we need to make ITO as low volume density and Oblique Angle Deposition is one of the easiest way for making nanostructures because of its shadow effects and low fabrication temperature without catalyst ( $< 200^\circ\text{C}$ ). Thus we successfully obtained that precisely designed graded refractive index ITO nanostructures by tilting E-beam chuck two steps (ie  $15^\circ$ ,  $85^\circ$ ) and applied it to planar silicon solar cells. These coatings can be widely compatible with any solar cells which has planar surfaces due to its low growth temperature ( $<200^\circ\text{C}$ ). But in the point of view of industrial silicon solar cell

fabrication, micro pyramid surface texturing to minimize Fresnel reflection has been widely adopted for high efficiency. To be compatible with conventional surface texturing technology, GRIN nanostructured ARC coating is deposited on the micro pyramid either.

### 3.2 Experimental processes of planar silicon solar cell with GRIN nanostructures.

#### 3.2.1 Formation of high refractive index Nanorods

High refractive index Indium Tin Oxide Nanorods were successfully deposited on planar silicon surface using conventional e-beam evaporator. To make dense layer, we need to give flux at low incident angle. In this study Optimum angle for dense nanorods is  $15^\circ$  that exhibits minimum reflection spectrum in broad range of wavelength (300-1100nm) which is described in Fig11. At incident angle lower than  $15^\circ$ , dense thin film like morphology is observed by SEM and its reflectance is increasing because of losing graded refractive index profiles. The fabrication temperature is above  $200^\circ\text{C}$  that cause self-catalyst Vapor Liquid Solid(VLS) growth mechanism. Under  $200^\circ\text{C}$  self-catalyst Vapor Liquid Solid (VLS) growth system is not adequately caused so that the morphology is not well controlled which means we cannot control the porosity of nanostructures. By combining Self catalyst Vapor Liquid Solid (VLS) growth mechanism and Oblique angle deposition, we can minimize surface reflection . Fig .11 describes conventional oblique angle deposition.

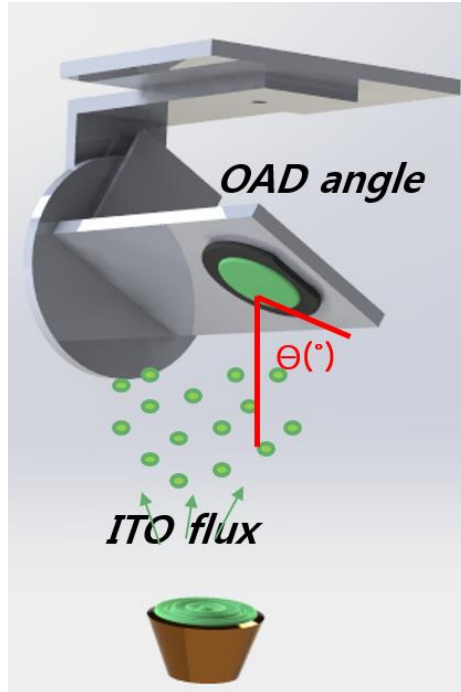
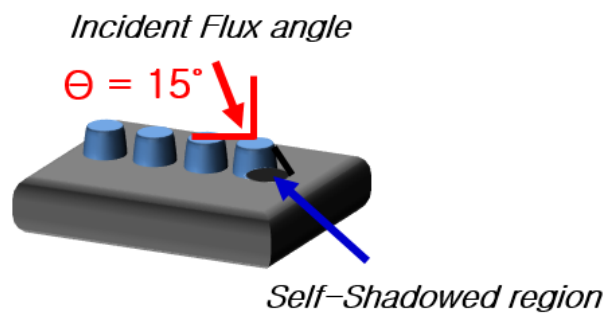


Fig11. Schematic illustration of Oblique angle deposition using e-beam evaporator

- *High Incident Flux angle : Nanorods*



- High density
- Small self-shadowed region

Fig12. Schematic illustration of High refractive index Nanorods formation

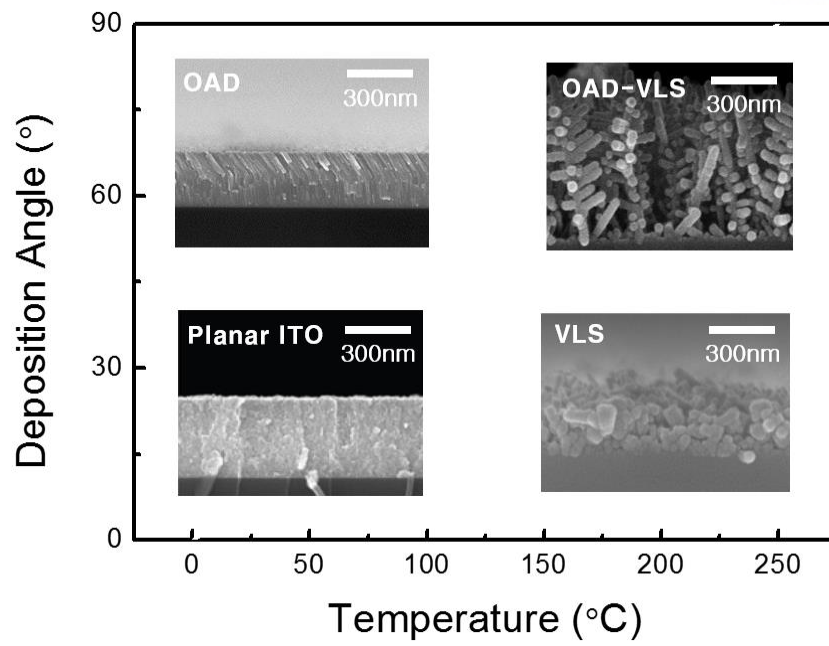


Fig13. Self-catalyst Vapor Liquid Solid growth with Oblique Angle Deposition

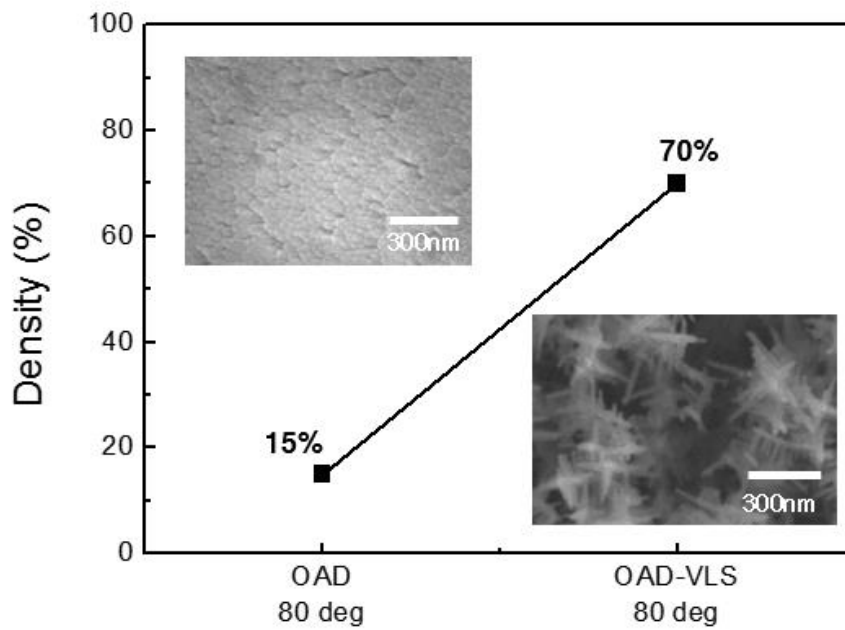
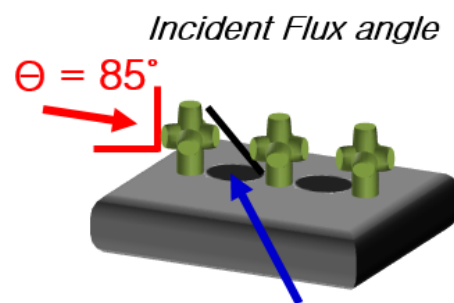


Fig14. Density distribution compared to OAD and OAD-VLS

### 3.2.2 Formation of low refractive index nanobranches

To make Graded refractive Index profile which can light propagating to medium, low refractive index material is needed. But there has been suffered from lack of low refractive index materials under 1.5. Fortunately, Oblique angle deposition using e-beam evaporator can break these deficiency by increasing porosity using self-shadowed region. Although these benefits, it is hard to make Graded refractive index profiles using only one materials due to difficulty of extremely porous nanostructures. So Schuberts et al group has been applied high refractive index materials ( $\text{TiO}_2$ ) and low refractive index materials ( $\text{SiO}_2$ ) using oblique angle deposition in achieving graded refractive index profiles. In this study we can obtain low refractive index nanostructures with incident angle at  $85^\circ$  using one materials of bulk ITO by combining Self-catalyst Vapor Liquid Solid (VLS) growth mechanism and shadow effect from E-beam Oblique angle deposition. As a results we can obtain extremely low refractive index 1.1

- *Low Incident Flux angle : Nanobranches*



- Low density *Self-Shadowed region*
- Large self-shadowed region

Fig 15. Low refractive index nanobranches formation

### 3.2.3 Graded Refractive Index(GRIN) Nanostructure formation on planar silicon

Graded Refractive Index profile can be easily obtained using linearly increased flux incident angle during e-beam evaporation of ITO with its novel growth mechanism. While changing flux incident angle, these nanostructures morphology can be changed from dense nanorods to porous nanobranches

which means high refractive index in bottom dense nanorods to low refractive index in nanobranches. This procedure is one of the easiest way to make GRIN structures with single materials and single steps with only inclining flux incident angle. After GRIN structure deposition additional annealing procedure is added to make ITO nanostructures transparent using Hot plate at 350°C, 10min.

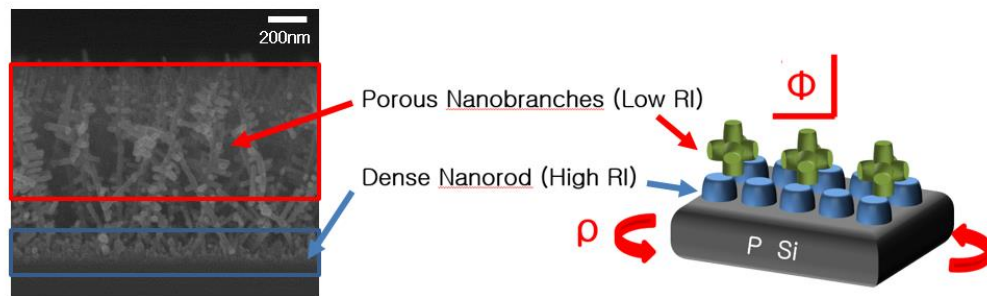


Fig16. Schematic illustration of Graded Refractive Index Anti-reflection coating using Self-catalyst Vapor Liquid Solid (VLS) growth mechanism and shadow effects using Oblique angle deposition

### 3.2.4 Fabrication of planar silicon solar cell with GRIN nanostructures

To adapt Graded refractive index structures, we have fabricated planar silicon solar cells with rapid thermal processing technique. Rapid thermal annealing process is one of the most easiest methods to make P-N junction because of its fast and simple procedures. Detail procedures are described below fig 17. First spin coating phosphorus solution to target silicon. For P-N junction different types of dopants compared to target silicon is used for doping. The Spin on dopant (SOD) solution is purchased from filmtronics (USA, P509). After spin coating SOD solution as 3000rpm for 30s, following soft baking on hot plate 200°C during 20minutes to eliminate remaining organic solvent. After soft backing spin coated silicon substrate is inserted to rapid thermal annealing chamber following 900°C 30s annealing. The temperature increasing time is 30s and plateau time is 30s following nature air cooling. After annealing, to eliminate the phosphosilicate glass layer, annealed wafer is immersed to buffered oxide etch (BOE) for 20 minutes. After remove phophosilicate glass layer, emitter sheet resistance is measured as 100 Ω/sq. The sheet resistance is key parameter for emitter characterization. After formation of n+ emitter in p silicon, bottom metal contact and top metal contact is deposited using conventional photolithography. The top grid pattern is designed based on common finger grid optimization methods



and its specific contact resistance is also measured using conventional Transmission Line Method (TLM) pattern design which is commonly used that gives information of annealing temperature of ohmic contact using Rapid Thermal Annealing. (300°C, N<sub>2</sub> 1min).

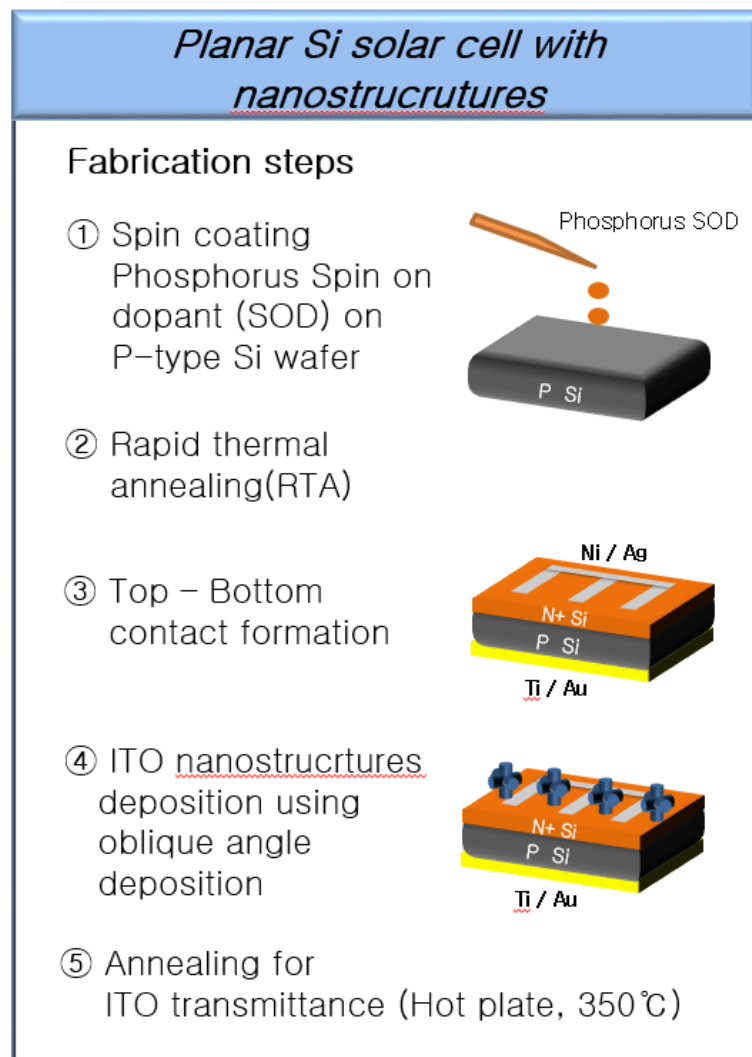


Fig17. Process flow chart making planar silicon solar cells with GRIN nanostructures

### 3.3 Experimental processes of textured silicon solar cell with GRIN nanostructures

### 3.3.1 Formation of GRIN Nanostructures on micro pyramid textures silicon

We investigated Graded Refractive Index Nanostructures on planar silicon surfaces. But in practical point of view, conventional micro pyramid texturing is used to eliminate surface Fresnel reflection for industrial level of silicon solar cell fabrication. Due to optimized pyramid angle  $55^\circ$  self - induced oblique angle deposition is caused automatically. Fig 18 displays optimal textured pyramids of SEM images. Thus we choose deposition angle  $0^\circ$  while elevating growth temperature up to  $200^\circ\text{C}$ .

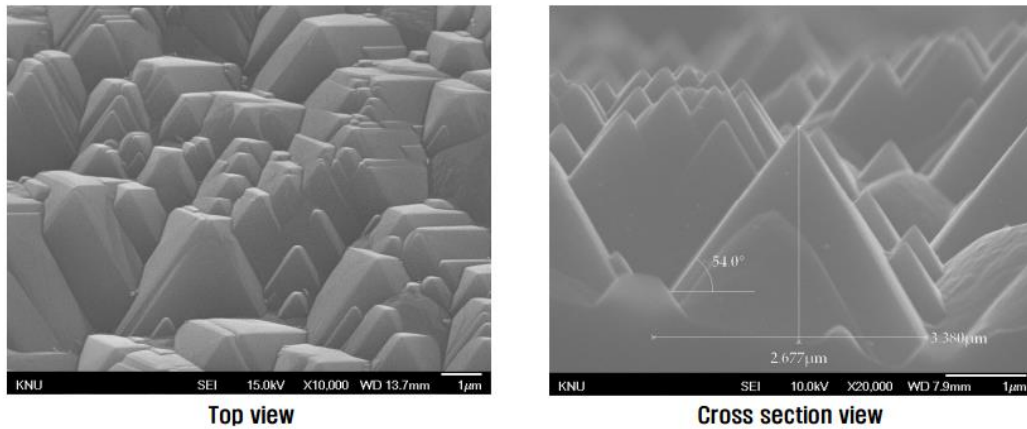


Fig. 18 Optimal micro pyramid structure for industrial level of silicon solar cell

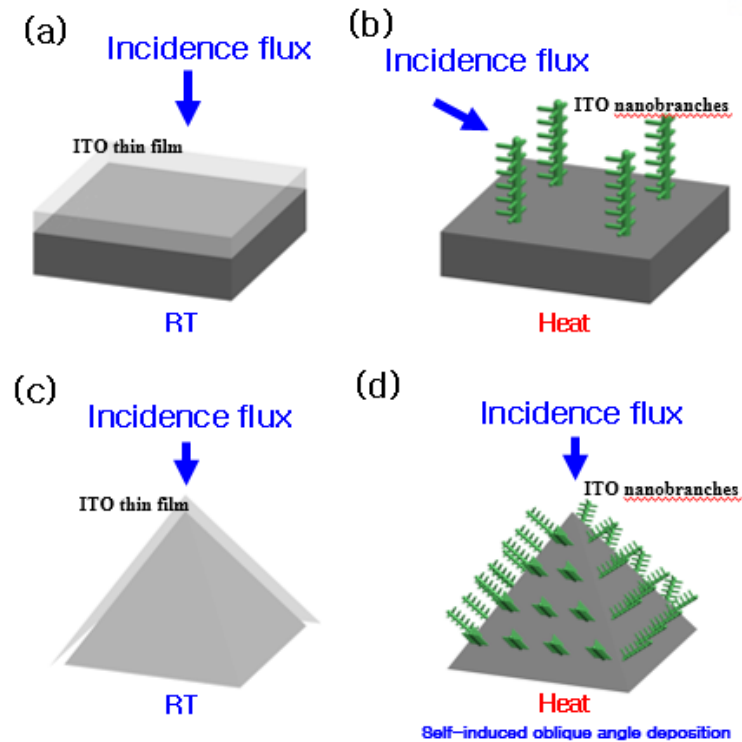


Fig. 19 Self induced shadow effect in textured silicon solar cell

### 3.3.2 Textured silicon solar cells fabrication with GRIN Nanostructures

In industrial level, silicon solar cell is texturized to reduce surface Fresnel reflection almost 40% for polished silicon. For texturization, Isopropanol based KOH etching solution is used to obtain pyramid angle as  $55^\circ$ . After texturization, conventional belt furnace is used to doping for n+ layer as  $\text{PoCl}_3$ . After  $\text{PoCl}_3$  doping, the emitter sheet resistance was measured as  $60 \Omega/\text{sq}$ . After emitter formation, conventional Al paste which acts both bottom metal contact and back surface field that eliminates back side of minority carriers for preventing recombination. As a results  $J_{sc}$ ,  $V_{oc}$  and Fill Factor are lightly increased. After screen printing of Aluminum paste, the solar cell is annealed using conventional belt furnace at  $600^\circ\text{C}$  45min. After bottom contact formation, top contact Ni(25nm) Ag(300nm) is deposited conventional e-beam evaporation and following annealing using rapid thermal annealing system at  $300^\circ\text{C}$ , 1min  $\text{N}_2$  ambient. After ohmic contact of top electrode, Indium Tin Oxide (ITO) GRIN

Nanostructures are deposited with varying thickness. Fig 16 describes detail process flow chart of micro textured pyramid silicon solar cells with GRIN Nanostructures.

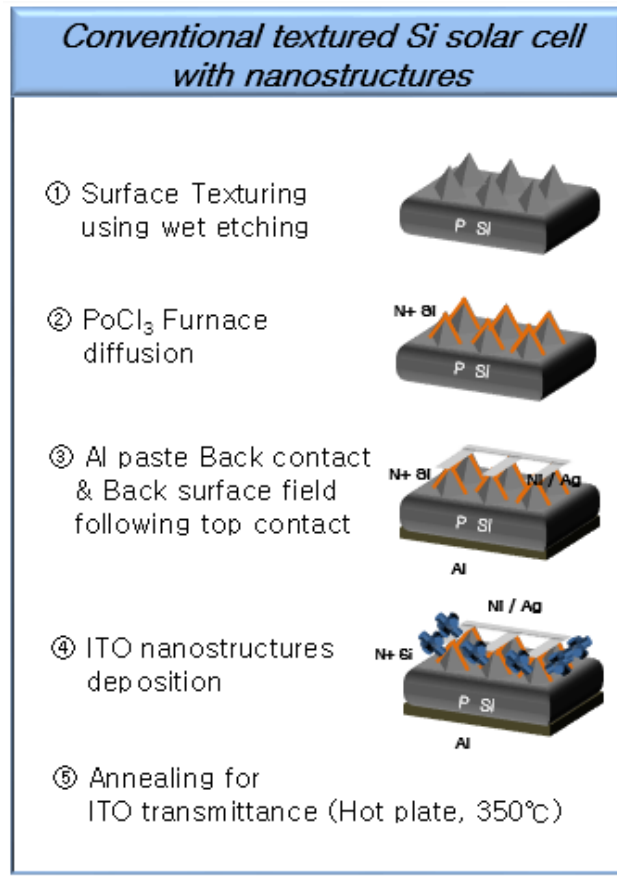


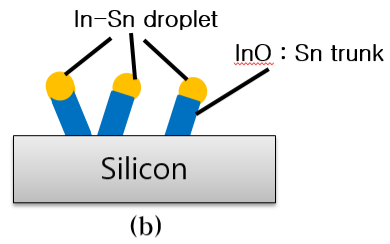
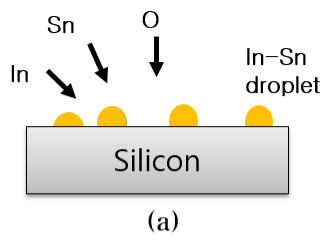
Fig20. Process flow chart making conventional textured silicon solar cells

### 3.4 Results and discussions

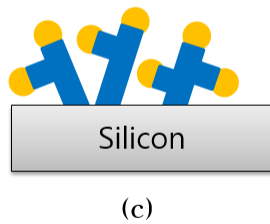
#### 3.4.1 GRIN ARC with planar silicon solar cells

##### 3.4.1.1 XRD and TEM analysis of GRIN Nanostructures

To demonstrate ITO based Nanostructured growth mechanisms. We have measured XRD, HR-TEM, and SEM. By observing droplets on the top of the branches in SEM images as can be seen in fig 21, we can confirm that our nanostructure is grown through Self-catalyst Vapor liquid Solid (VLS) growth mechanism. Details of growth steps is described below in fig 21. First Indium, Tin, Oxygen atoms are reaches heated substrate which is higher than melting point of indium. Second vapors are preferentially absorbed onto the liquid droplet due to high accommodation coefficient of liquid. Third, new droplets are formed on the side of trunk surface when the degree of vapor phase becomes higher.



- Indium, tin, oxygen atoms are reached substrate heated to higher temperature than the melting point of indium ( $> 155^{\circ}\text{C}$ )
- Vapors are preferentially absorbed onto the liquid droplet due to high accommodation coefficient of liquid



- New droplets are formed on the side of trunk surface when the degree of vapor phase becomes higher.

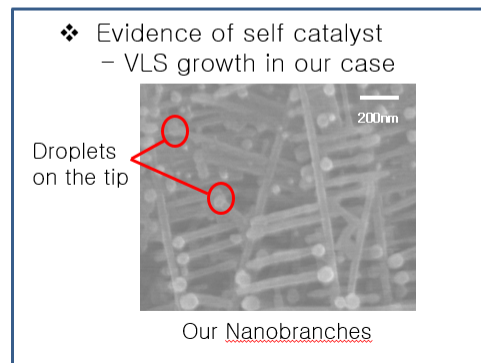


Fig 21. Schematic illustration of Self-catalyst Vapor Liquid Solid Growth mechanism

As can be seen in fig X, first deposited dense nanorods exhibits same preferential peak (222) with dense ITO. But while growing nanobranches the preferential peak is changed to (400). This results is good agreement with HR-TEM results. In fig X, Nanobranches`s trunk preferential peak is (400) and we can see the same electron diffraction pattern between Zone 1. Trunk and Zone 2 small Branches. Furthermore the interfaces of crystal lattice between trunk and small branches is perfectly aligned which means the epitaxial relationship between trunk and small branches and our nanostructure is single crystal.

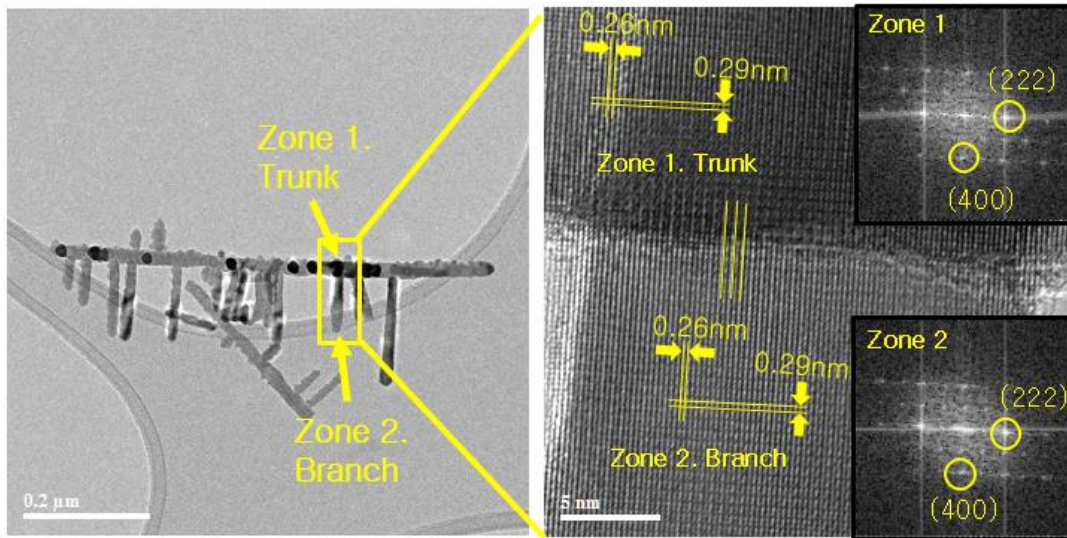


Fig. 22 HR-TEM images and electron diffraction pattern of Nanostructures

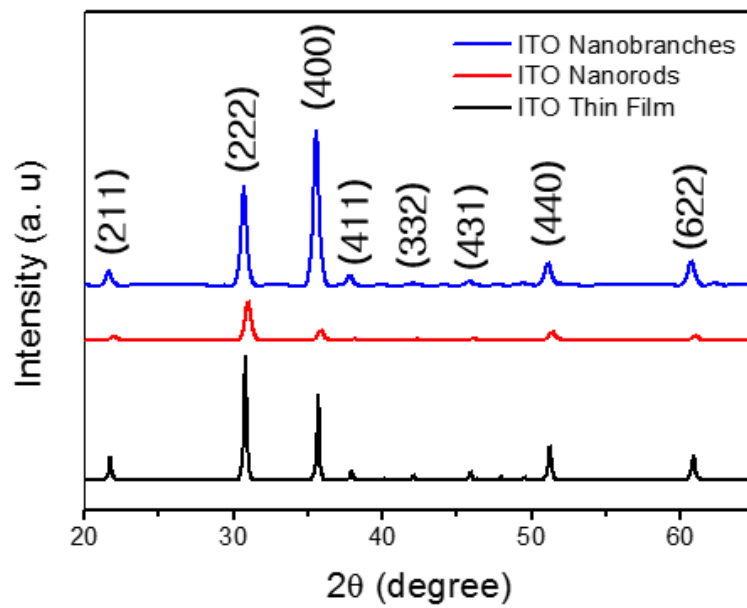


Fig. 23 XRD diffraction pattern of ITO thin film, Nanorods and Nanobranched

### 3.4.1.2 SEM Images and Optical properties of GRIN Nanostructures

The Graded Refractive Index profile of nanostructures are divided into two components. The first one is dense Nanorods which is deposited at extremely low flux incident angle of  $15^\circ$  for high refractive index. And then for low refractive index, flux incident angle is increased up to  $85^\circ$ . First deposited dense Nanorods of SEM images and its optical properties are described in fig 24. We can observe the decreasing Nanostructure density with increasing flux incident angle change between  $7^\circ$  to  $75^\circ$  by SEM images.

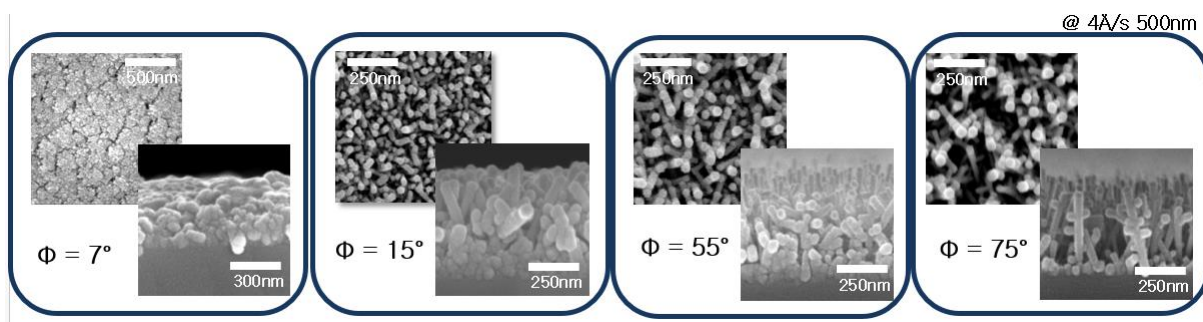


Fig 24. Formation of Indium Tin Oxide (ITO) nanorods on planar silicon

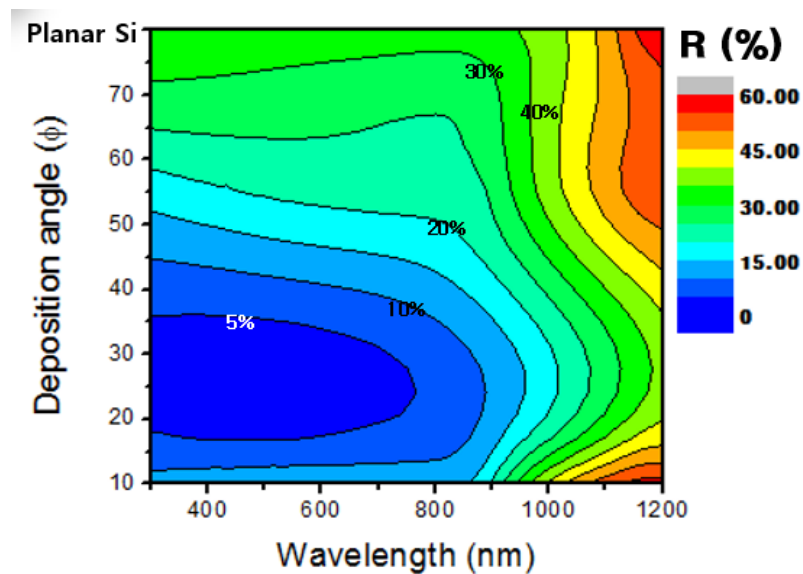


Fig 25. Total reflectance spectra with varying thickness and wavelength

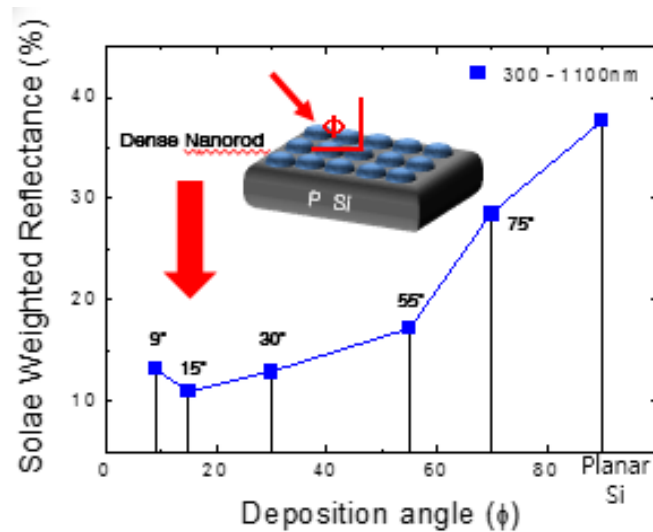


Fig 26. Total Solar Weighted Reflectance with varying deposition angle

In fig26 the porosity of deposited film is gradually increased with increasing flux incident angle that is clearly shown by SEM images. Also with increasing porosity, its total reflectance is increased. This results clearly gives that the solar weighted reflectance is optimized at the low flux incident angle 15° because of refractive index matching between air (1) and silicon (3.5). The solar weighted reflective index is lowest at given angle at 15° as 10% and it is slightly increasing under 9°. The increased solar weighted reflectance at 7° is explained that under critical angle at 15° the oblique angle deposition could not work because there were no more presence of self-shadowed region between droplets. Thus deposited nanostructures are losing its unique Graded refractive index matching properties under and upper 15°.

To optimize nanorods, we need to consider flux incident angle, film thickness, deposition rate. First we optimized deposition angle as 15° and then actual film thickness is considered. By changing film's thickness 200nm to 500nm, the solar weighted reflectance is optimized film thickness 200nm as 9%. Third, we consider deposition rate. By changing deposition rate, we can observe the peak shift between 600nm and 1000nm with changing deposition rate. When deposition rate is 1Å/s and 4Å/s the lowest reflectance is observed at 600nm as 3% but relatively high reflectance is observed at 1000nm as 20%. But when deposition rate is 4Å/s, 600nm wavelength area reflectance is relatively higher than 1000nm



but total solar weighted reflectance is lowest among all deposition rates. Thus we optimized deposition angle at  $4\text{\AA}/\text{s}$ .

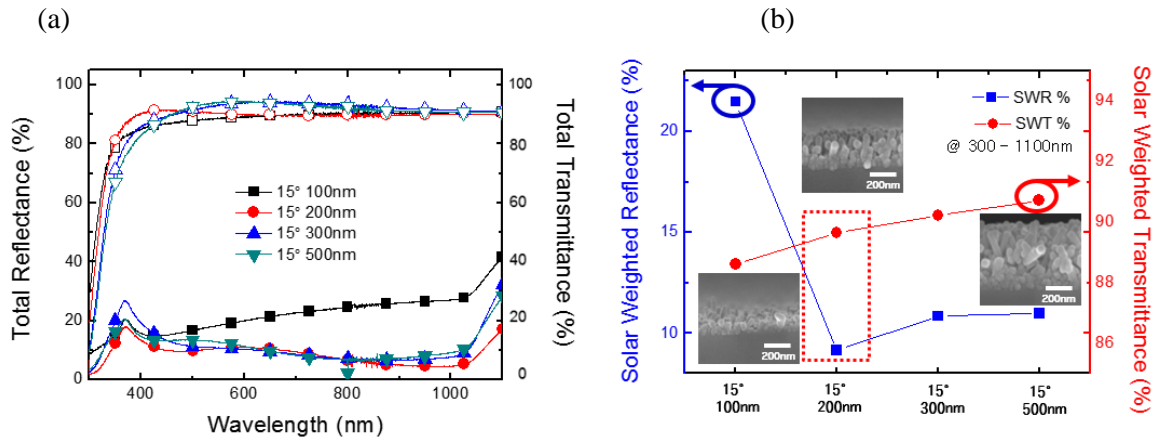


Fig 27. (a) Total reflectance and transmittance spectrum with varying Nanorods thickness, (b) Solar weighted reflectance and solar weighted transmittance with varying Nanorods thickness

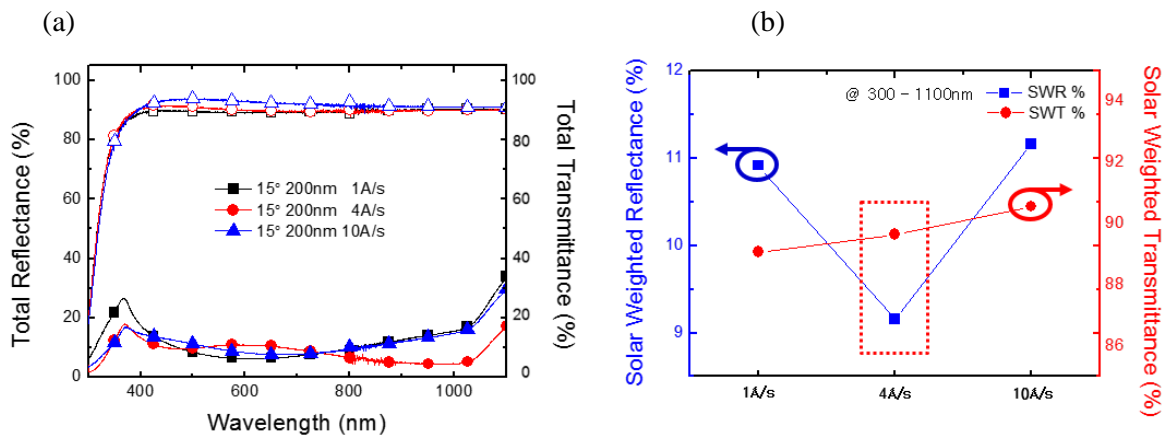


Fig 28. (a) Total reflectance and transmittance spectrum with varying deposition rates (b) Solar weighted reflectance and solar weighted transmittance with varying deposition rates

reflectance and solar weighted transmittance with varying deposition rates

For low refractive index, we need to deposit nanobranched structures which have a refractive index of 1.1 ~ 1.3. At a high flux incident angle of 85°, porous nanobranched structures were grown, and their height is well controlled with increasing deposition time without any trade-off relationships. Many research groups have reported that nanostructures fabricated by wet and dry etching have a high aspect ratio, but they have trade-off relationships between electrical properties and optical properties because of etching damage. However, we made high aspect ratio nanostructures without any electrical and optical loss. The optical properties and morphologies of the deposited nanobranched structures are described below. Before optimizing nanobranched structures, we explored morphology engineering of nanobranched structures for unique film properties of haze. By simply rotating the e-beam chuck ( $\rho = 360^\circ$ ) 2.5 times per minute, the rotated nanobranched structures exhibit a higher haze ratio compared to non-rotated films, especially at a wavelength of 550 nm, from 40% to 15%. The rotated film has been experienced with continuous flux from all angles. Thus, there are 4 legs compared to 3 legs in a non-rotated film. This phenomenon is explained in fig. 29, 30

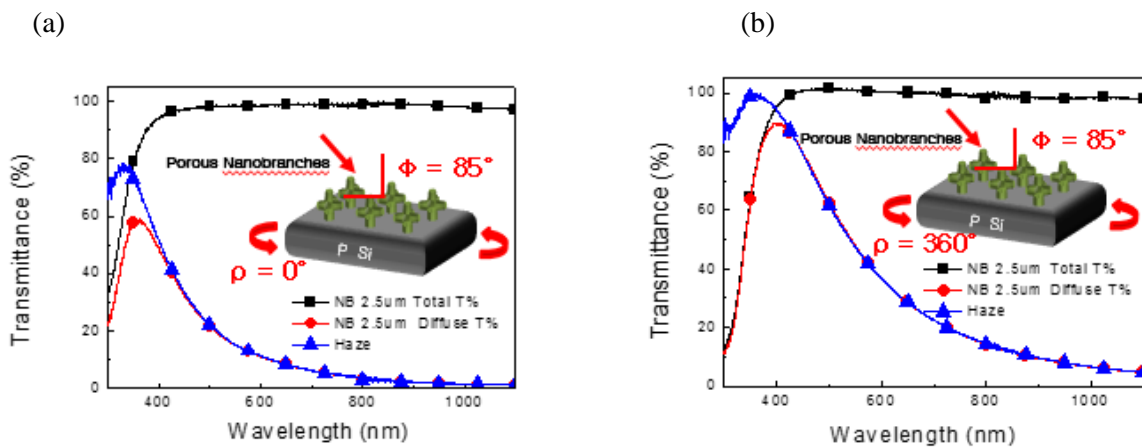


Fig 29. (a) Haze ratio of NB 2.5  $\mu\text{m}$  without substrate rotation (b) Haze ratio of NB 2.5 $\mu\text{m}$  with substrate rotation

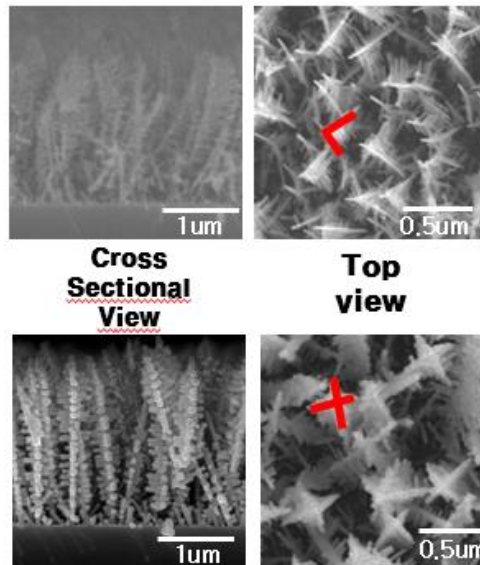
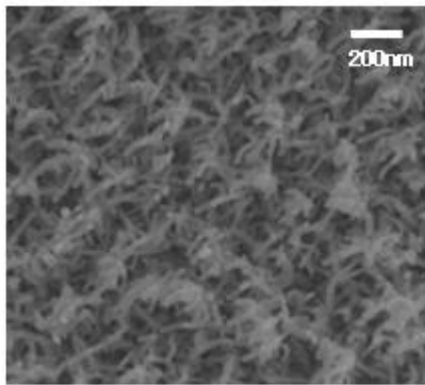
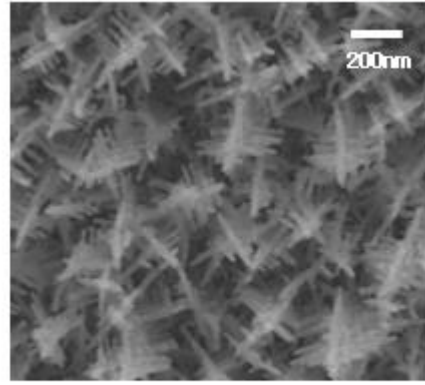


Fig. 30 (a) SEM images of NB 2.5  $\mu\text{m}$  without substrate rotation (b) SEM images of NB 2.5 $\mu\text{m}$  with substrate rotation

With increasing film thickness and rotating substrate, branches are grown as periodic structure because of continuously given flux in all directions. So branches has one trunk along with several small branches. These morphologies are described by SEM image in fig.31, 32



**NB 500nm**



**NB 1μm**

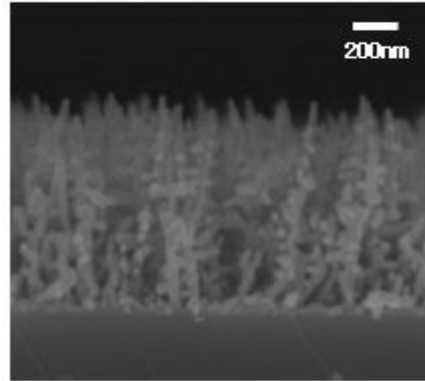
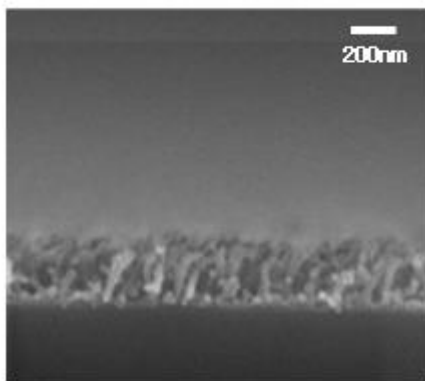
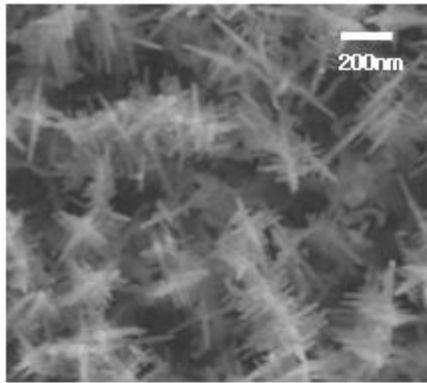
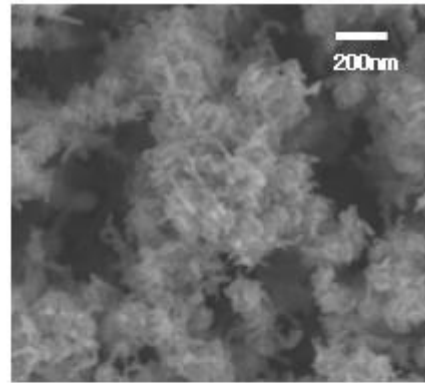


Fig 31. SEM images of nanobranches with varying thickness



**NB 2um**



**NB 3um**

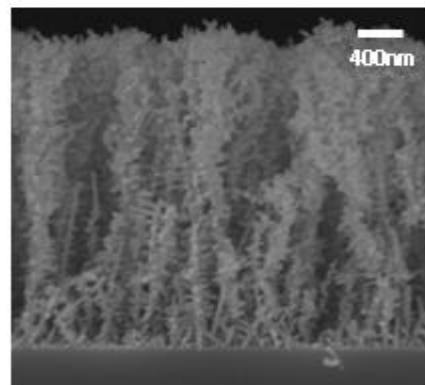
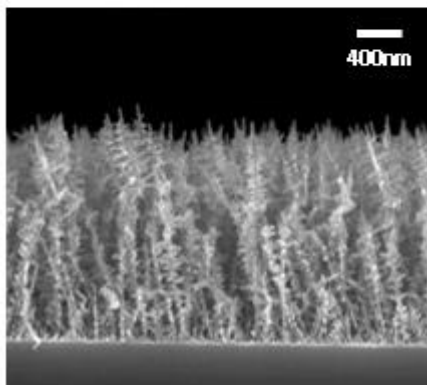


Fig 32. Morphologies of nanobranches with varying thickness

Nanobranches has its unique optical properties such as highly transparent, High Haze ratio  
 We can observe decreasing with increasing transmittance and reflectance values while increasing film thickness over 2um. Especially between nanobranches height 2um and 3um, these optical properties are significantly changed over 2um SWT is decreased to 97% to 91% and SWR is increased 16% to 19% from whole range between 300nm to 1100nm.

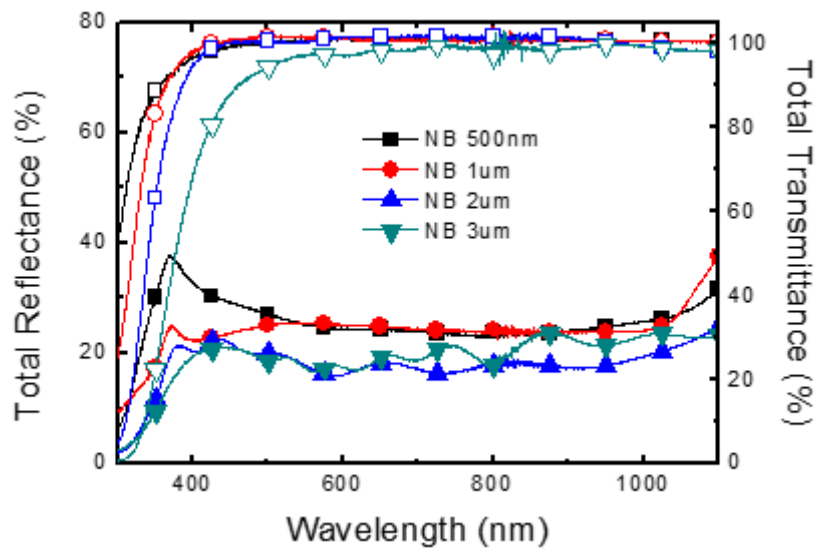


Fig 33. Total transmittance and reflectance spectra with varying nanobranches thickness

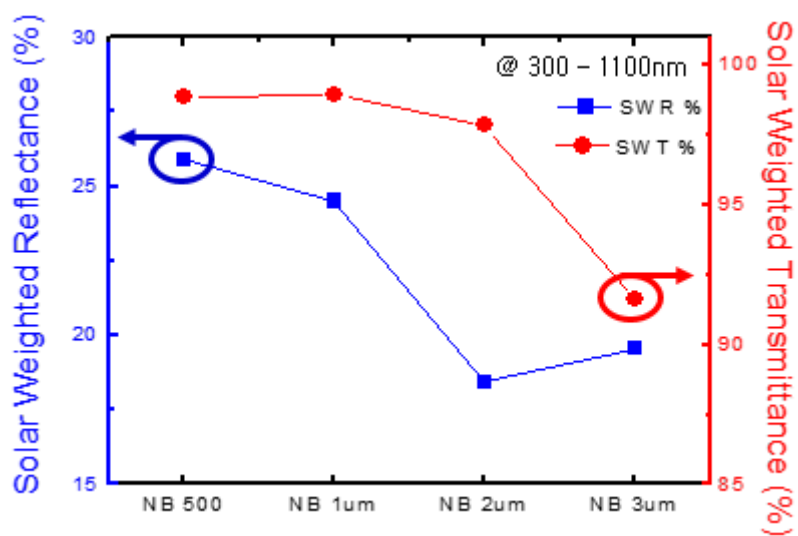


Fig. 34 Solar weighted reflectance and transmittance spectra with varying NB thickness

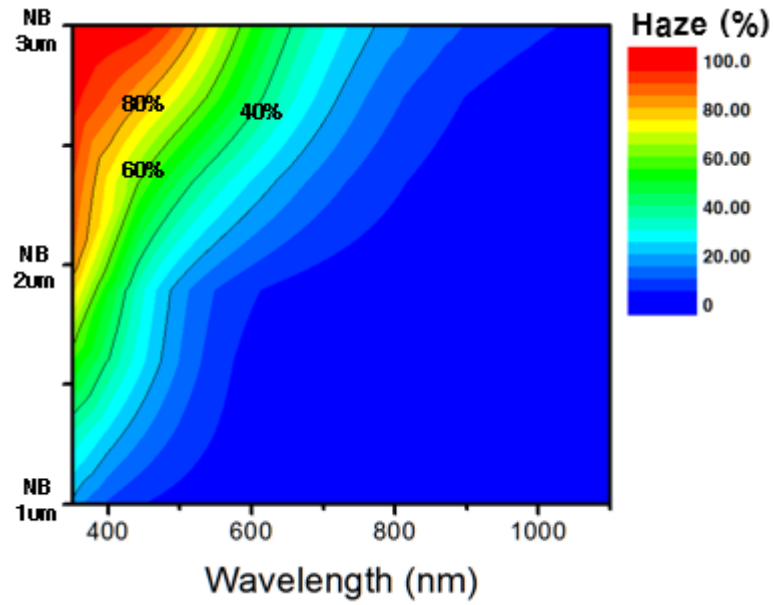


Fig. 35 Haze ratio with varying NB thickness

For making Graded Refractive Index structures, we unite both nanorods and nanobridges. First, deposited nanorods on the polished silicon and then nanobridges are formed on the nanorods. Fig36 Shows the Graded refractive index SEM images as cross sectional view and top view with varying thickness

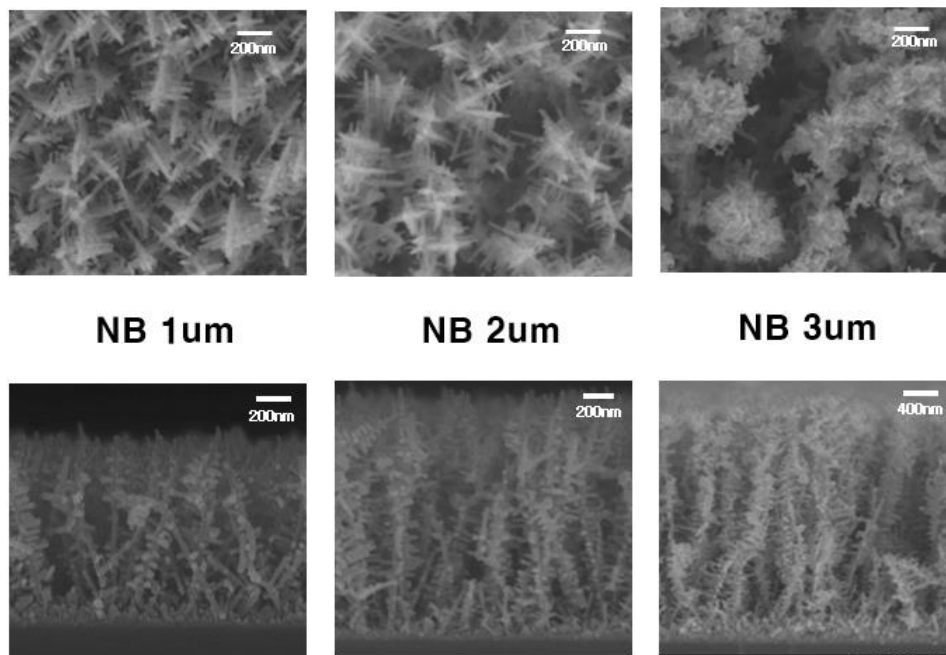


Fig. 36 SEM images of varying Graded refractive index fractal structures

Graded refractive index nanostructures are described in fig 37, 38. As expected with increasing nanobranches thickness, total reflectance and transmittance is decreased and increased below 2 $\mu\text{m}$ . But film thickness above 2 $\mu\text{m}$ , the solar weighted transmittance is significantly decreased from 95% to 90% while its reflectance is constant which means that absorption is occurred in nanobranches because of its high thickness. Also haze ration is similar trends and values compared to only nanobranch case.

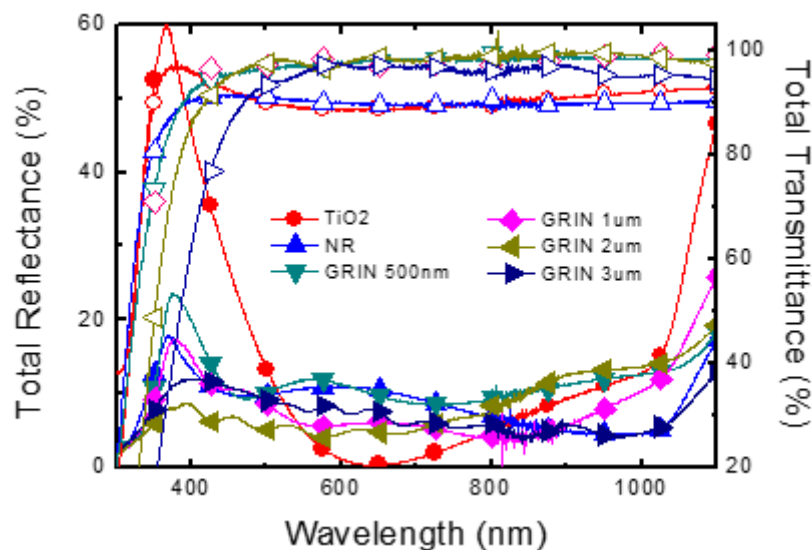


Fig 37. Total transmittance and reflectance spectra with varying GRIN thickness



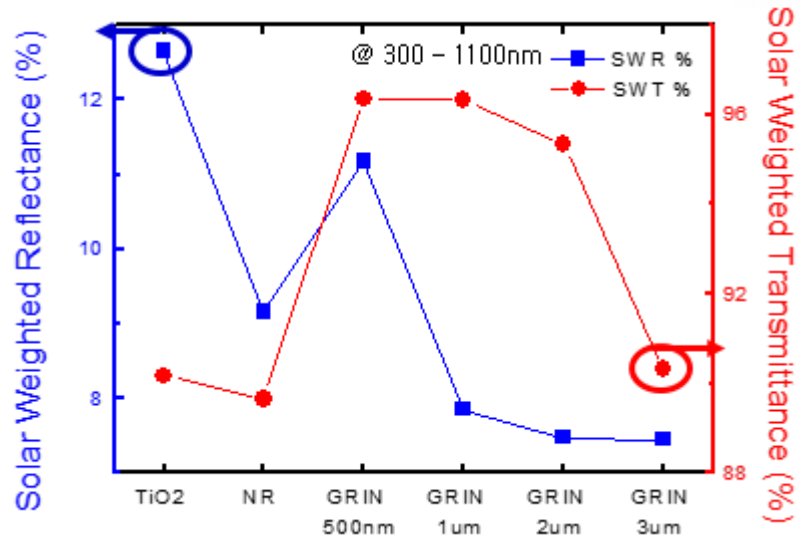


Fig 38. Solar weighted reflectance and transmittance spectra with varying NB thickness

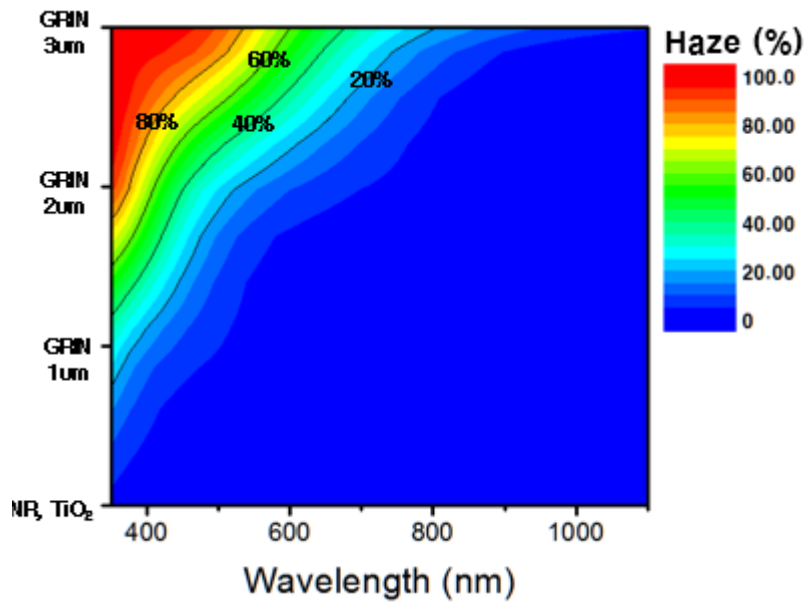
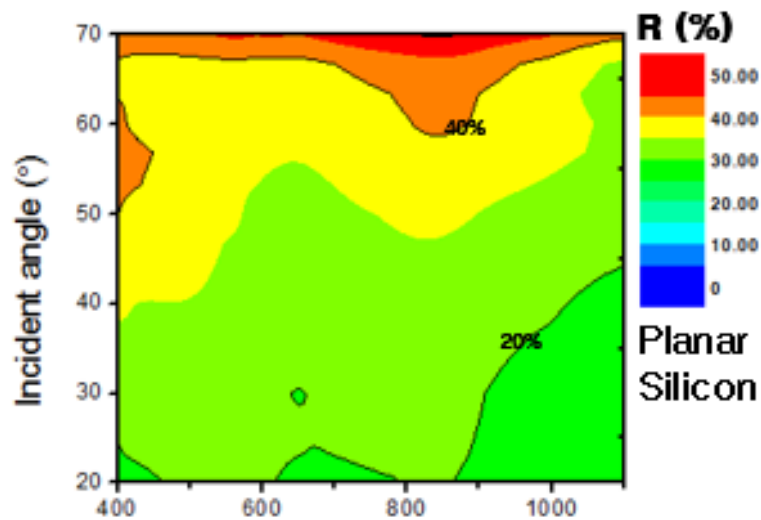
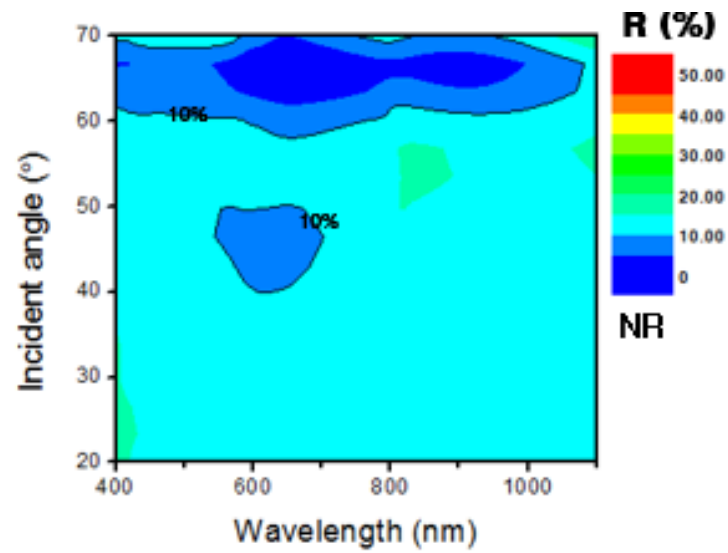
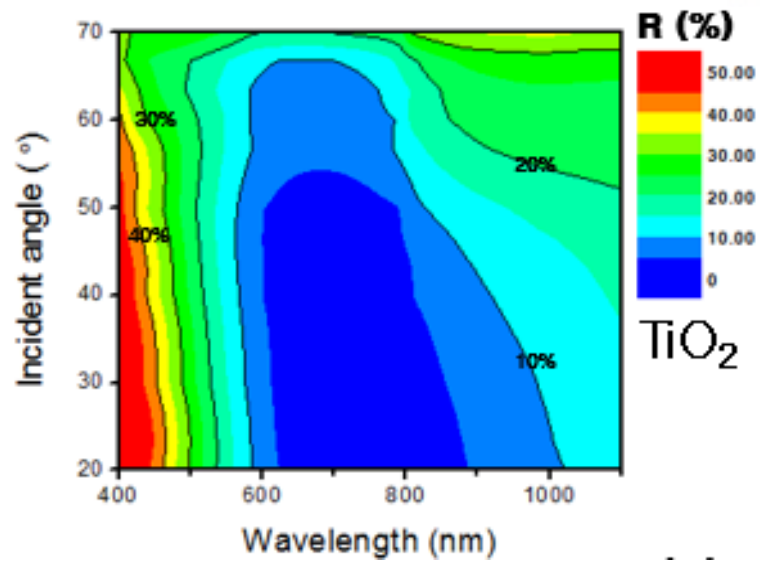


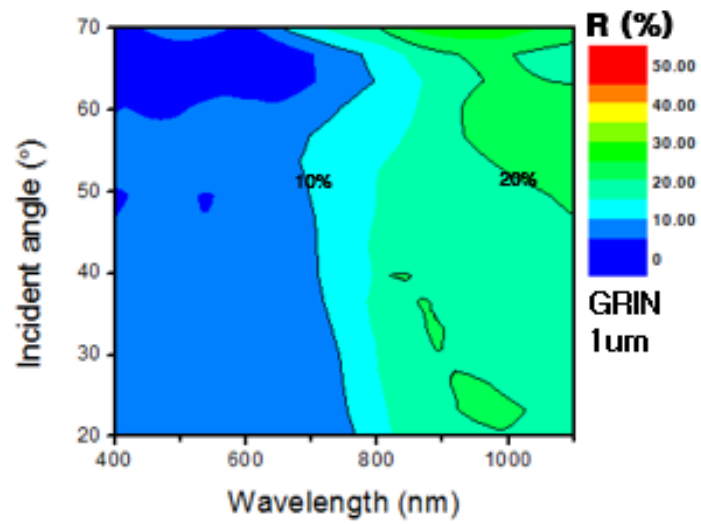
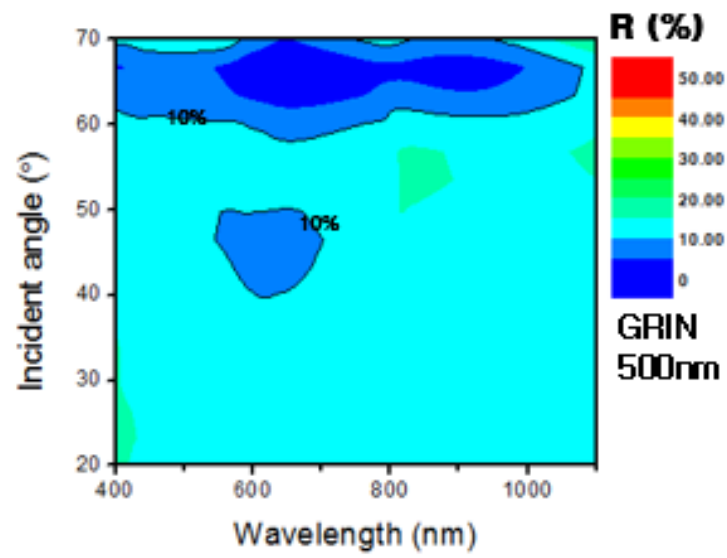
Fig 39. Haze ratio with varying GRIN thickness

To demonstrate the Omnidirectional antireflections. We have measured variable reflectance as a function of incident angles from 20° to 70°. The results are described below fig 40. In planar silicon case its reflectance is increased to average 50% at incident angle 70°. These tendency is also observed in conventional antireflection TiO<sub>2</sub> Case. Although specific region 500~600nm for lowest reflection

area, it has been increased to 20% at incident angle 70°. Even if single antireflection coating reduce specific region of reflection the other region maintains high reflection such as 300 – 500nm and 800 – 1100nm. This means that conventional single layer antireflection cannot overcome angular responses. In nanorods case, average reflectance 11~12% for broad band and omnidirectional directions. But it is still not sufficient for its high reflectance for entire region. This point can be solved by depositing nanobranches on the nanorod. With increasing nanobranches thickness, Graded refractive index fractal structures reveals low reflection among broadband and omnidirection region which is well fitted to Haze ratio tendency. With increasing nanobranches thickness, the scattered region (300 to 800nm) has losen its specular reflection condition.







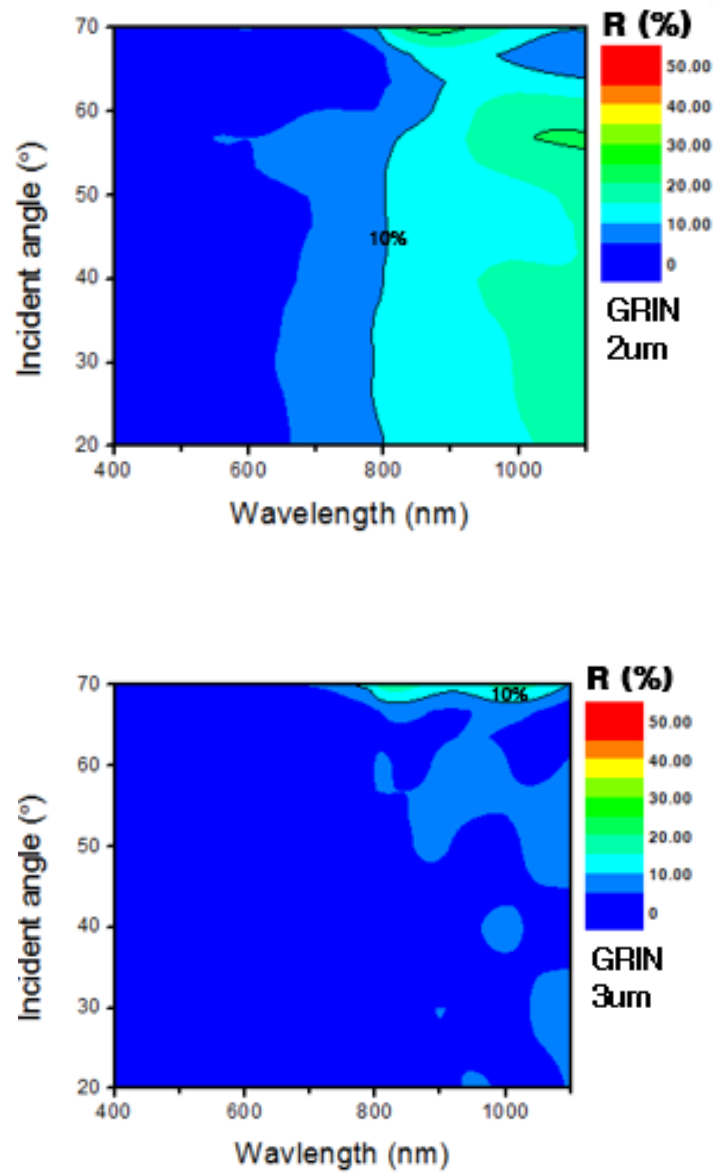


Fig40. Variable incident angle of reflectance with varying GRIN thickness

### 3.4.1.3 Electrical properties of planar silicon solar cells with GRIN nanostructures

To apply Graded refractive index structures, we fabricated planar silicon solar cell using spin on dopant. We adopt phosphorus dopant to p - type bulk silicon for making shallow emitter using rapid thermal annealing process. The sheet resistance is gradually decreased with increasing annealing temperature up to 1000°C. In annealing temperature 900°C, emitter sheet resistance is decreased below 100Ω/sq and then dramatically decreased with increasing temperature 1000°C.

Too low sheet resistance means that electrons could be captured from lattices on the highly doped emitter region. Also too high sheet resistance value reveals not enough doping which cannot make sufficient internal electric field. This sheet resistance value is directly connected to solar cell efficiency. As seen in fig41, at annealing temperature 800 °C insufficient doping cause lower power densities compared to 900°C. In 1000°C solar cell is significantly degraded because of leakage current in space charge region and quasi neutral region. We successfully fabricated 9% silicon solar cell only with p-n junction.

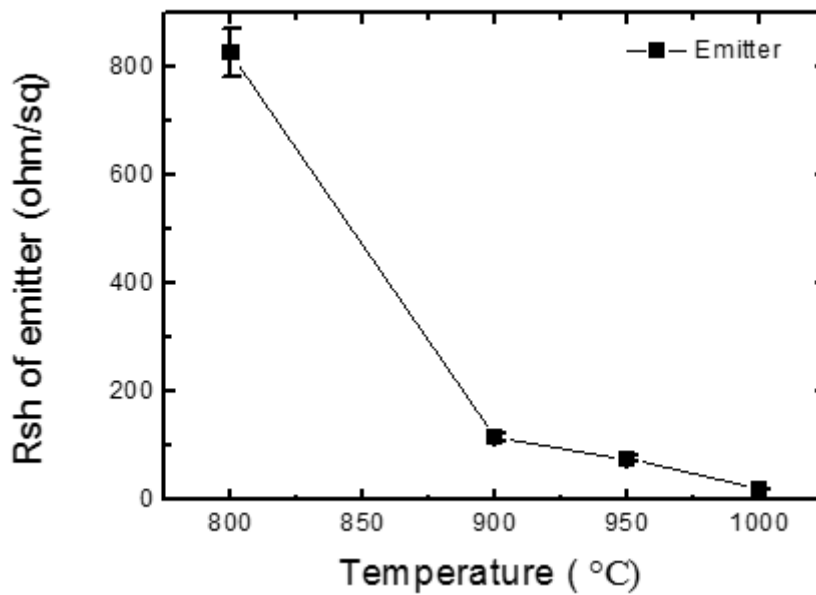


Fig 41. Sheet resistance of n+ emitter with varying annealing temperatures

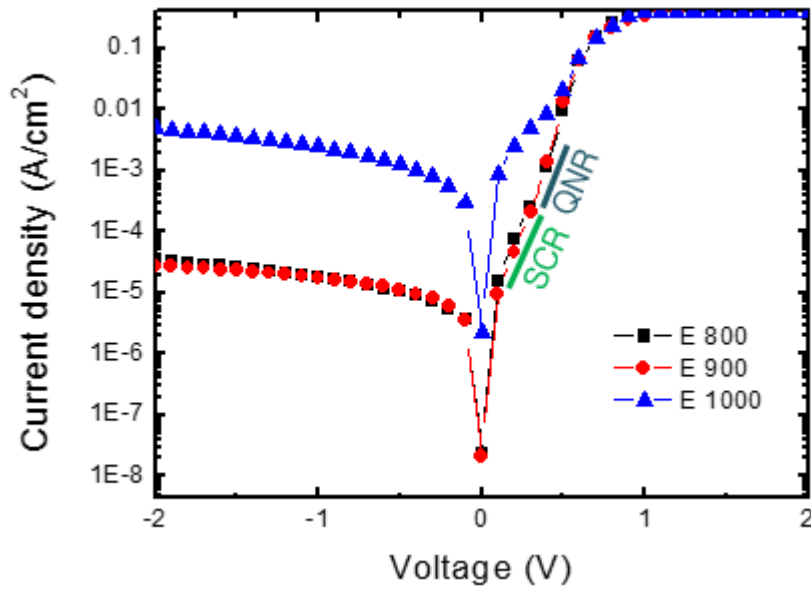


Fig 42. Dark current densities of solar cells with varying annealing temperatures

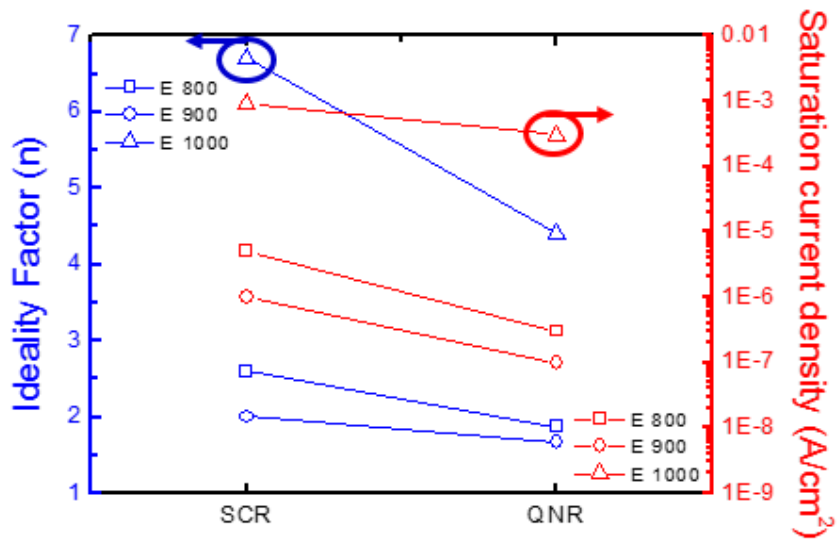


Fig 43. Ideality Factor and Saturation current densities with varying annealing temperatures

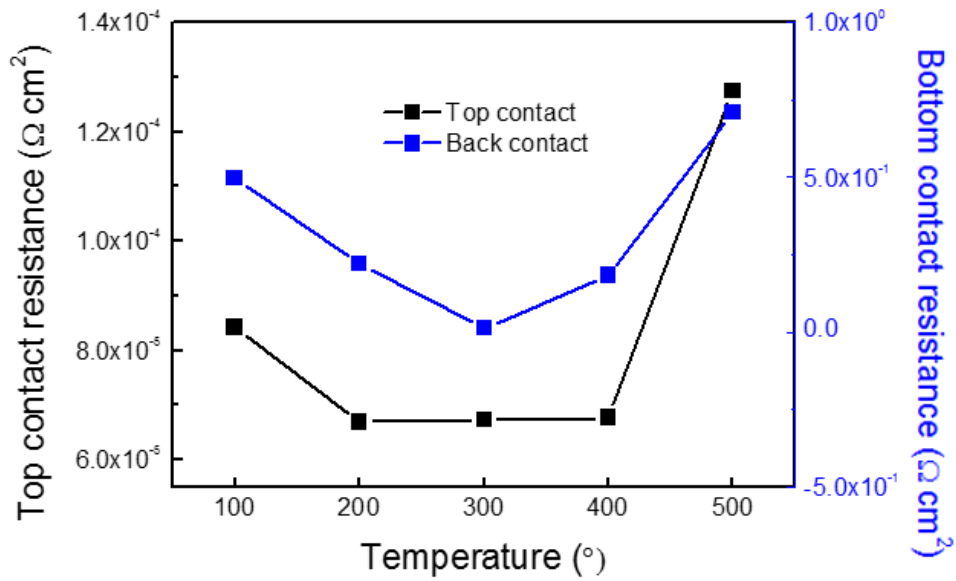


Fig. 44 Solar cell top and bottom contact resistances

	<u>Jsc</u> (mA/cm <sup>2</sup> )	<u>Voc</u> (V)	FF (%)	$\eta$ (%)
<b>E 800</b>	21.22	0.49	71.4	7.47
<b>E 900</b>	25.23	0.52	69.7	9.03
<b>E 1000</b>	22.21	0.47	50.8	5.33

Table 1. Solar cell parameters

Graded refractive index nanostructures are combined with silicon solar cells. J-V curved, Shunt and Series resistance is described in fig 47. When nanorods with silicon solar cells case, Jsc enhancement is 32% which is higher than TiO<sub>2</sub> and GRIN 500nm. With increasing GRIN thickness up to 1 $\mu$ m Jsc enhancement is 39% and efficiency enhancement is almost 50%. Increased fill factor is most impressive parameter because usually antireflection coating cannot increase solar cell fill factor even decreases it due to significantly increased Jsc. To investigate these effects we extract series and shunt resistance from measured I-V curves.



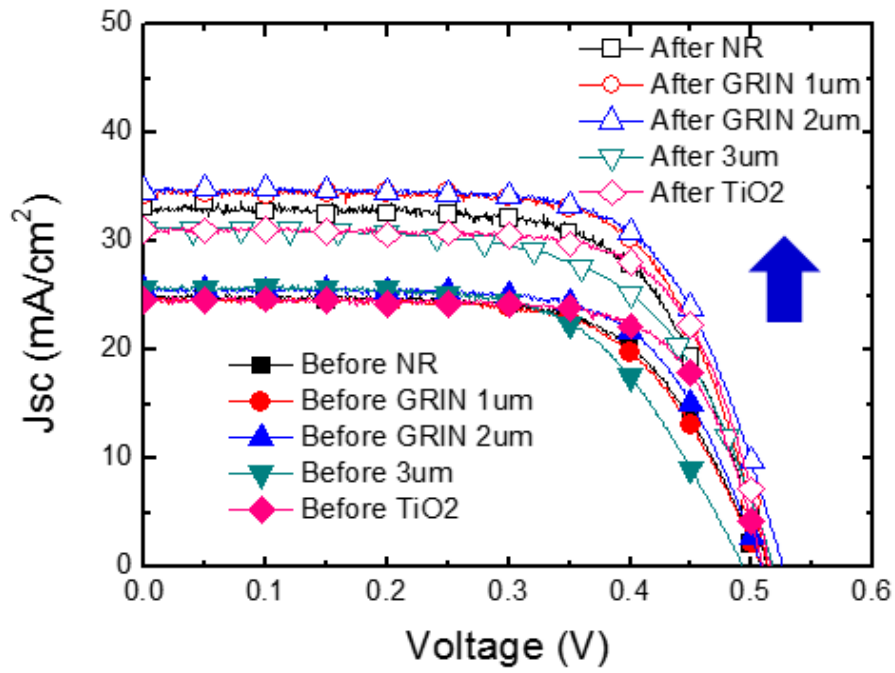


Fig. 45 Solar cell J-V characteristics with varying thickness of GRIN nanostructures

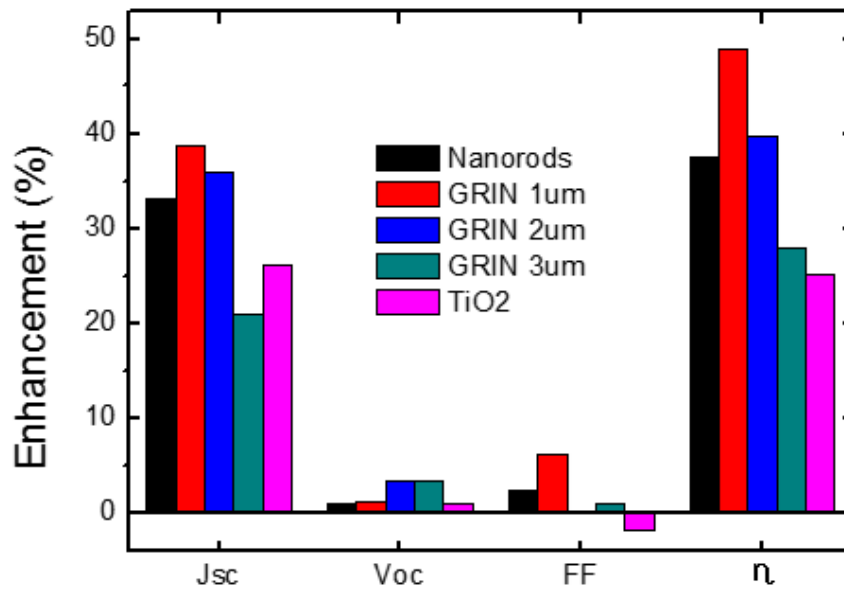


Fig. 46 Parameter enhancement factors of solar cells with varying GRIN thickness

*Before coating*

	<u>Jsc</u> (mA/cm <sup>2</sup> )	<u>Voc</u> (V)	FF (%)	$\eta$ (%)
NR	24.8	0.50	65.7	8.3
GRIN 1 $\mu$ m	24.8	0.50	65.0	8.2
GRIN 2 $\mu$ m	25.4	0.50	68.1	8.8
GRIN 3 $\mu$ m	25.7	0.49	62.3	7.9
TiO <sub>2</sub>	24.6	0.51	72.0	9.0

*After coating*

	<u>Jsc</u> (mA/cm <sup>2</sup> )	<u>Voc</u> (V)	FF (%)	$\eta$ (%)
NR	33.1	0.51	67.2	11.4
GRIN 1 $\mu$ m	34.3	0.51	69.0	12.2
GRIN 2 $\mu$ m	34.57	0.52	68.2	12.3
GRIN 3 $\mu$ m	31.1	0.51	63.0	10.1
TiO <sub>2</sub>	31.08	0.51	70.6	11.3

Table2. Solar cell parameters with varying GRIN thickness

By calculating Series and shunt resistance, we can conclude that these GRIN nanostructures can reduce series resistance while maintaining shunt resistance high value. We suspect that GRIN nanostructures affects emitter surface and reduce its sheet resistance. These results can be seen in fig . 47. Specific contact resistance is measured by conventional Transmission Line Method (TLM). We can achieve  $6.7 \times 10^{-5} \Omega\text{cm}^2$  in top contact before nanostructure annealing. To investigate reduced series resistance effects, we measured specific contact resistance before and after. After annealing hot plate  $350^\circ\text{C}$ , 1min no change is observed in contact resistance. So we can conclude ITO nanostructures influences entire series resistance.

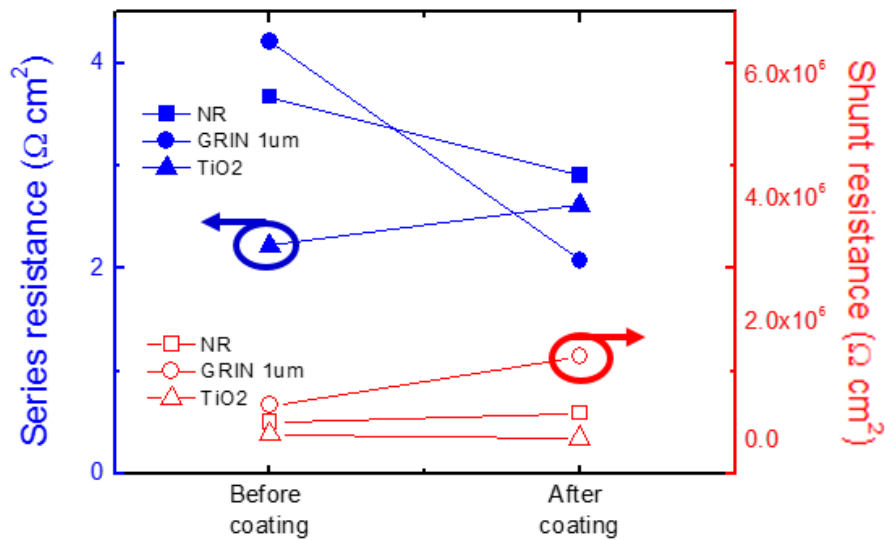


Fig 47. Series and Shunt resistance before and after GRIN coating

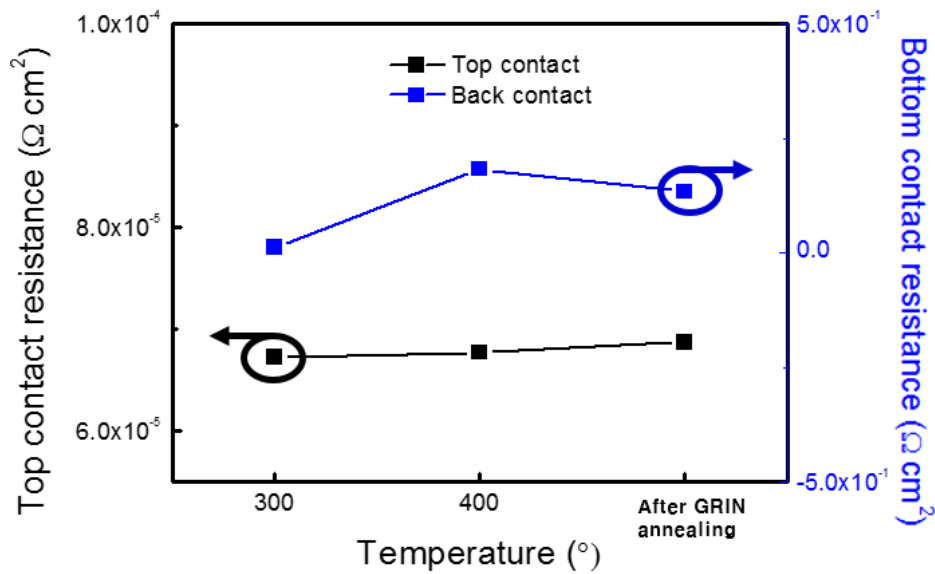


Fig 48. Top and bottom contact resistance before and after GRIN annealing

To demonstrate omnidirectional properties, we measured solar cell efficiency with varying incident light angle ( $0^\circ \sim 90^\circ$ ). As we expected angular response is increased with increasing GRIN thickness in fig 49. The best angular response is measured GRIN 3 $\mu\text{m}$ . But to know exact solar cell performance, thus we calculate annual power density by substituting meridian altitude of Seoul, Korea, 2014. Data is provided KASI, Korea. We can observe significantly increased annual power density in GRIN 2 $\mu\text{m}$  due to its omnidirectional enhancement. Unlike conventional solar cell parameter measurement result in fig39 GRIN 2 $\mu\text{m}$  reveals enhanced total power density 73.9% compared to 68.2% of GRIN 1 $\mu\text{m}$ . These results means conventional solar cell parameter measurement doesn't reflect angular response. So we concludes optimized GRIN thickness is 2 $\mu\text{m}$ .

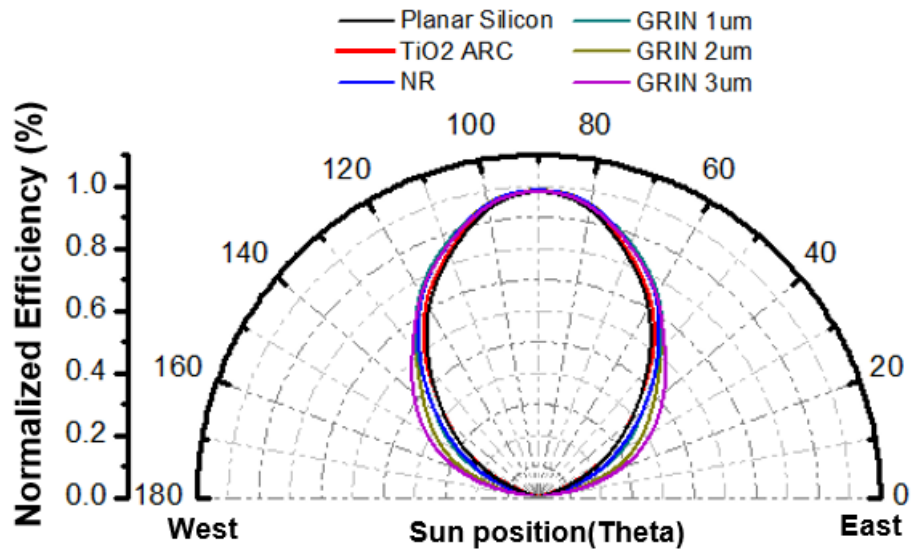


Fig49. Angular response of solar cell efficiency with respect to GRIN thickness

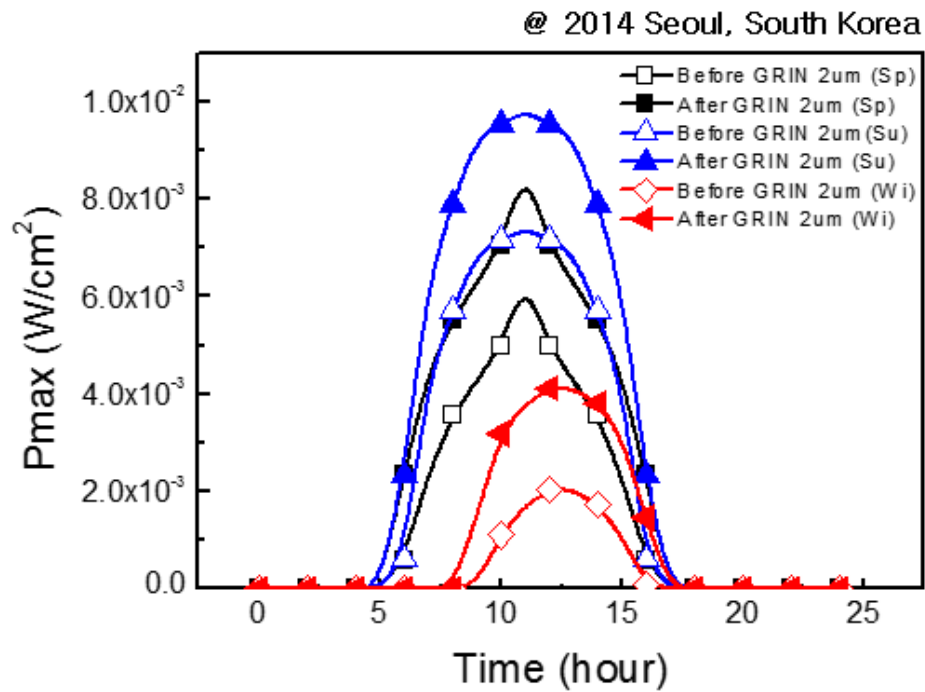


Fig50. Daily maximum power density with respect to time change

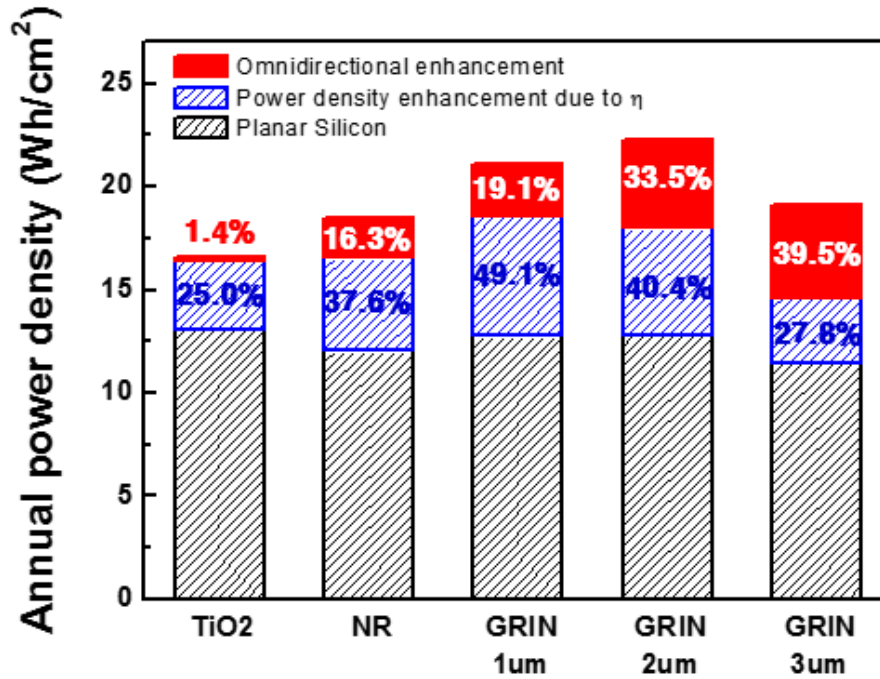


Fig 51. Annual power density with respect to power density enhancement and omnidirectional enhancement

### 3.4.2 ITO Nanobranches with conventional textured silicon solar cells

#### 3.3.2.1 SEM images and optical properties of GRIN Nanostructures

For the textures silicon solar cells nanobranches are characterized with varying thickness. Unlike planar surfaces case, these structures can make self induced oblique angle deposition. Detail SEM image are described below fig 52.

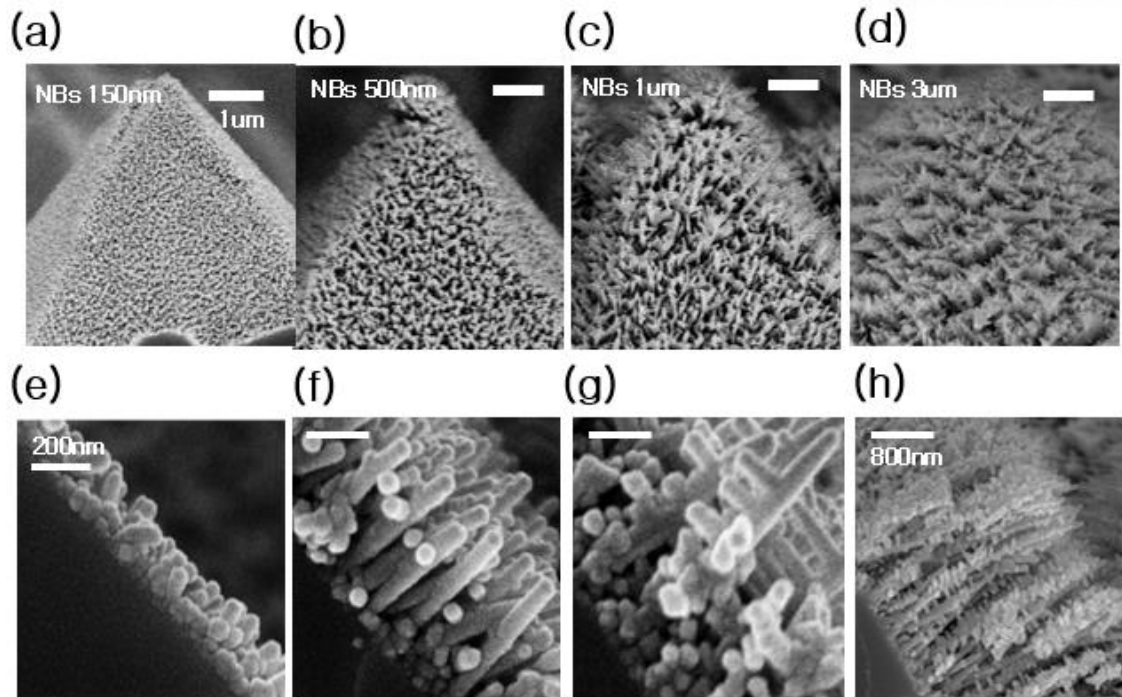


Fig 52. GRIN nanostructures on pyramid textures silicon with varying nanostructure thickness  
(a) NBs 150nm, (b) NBs 500nm, (c) NBs 1um, (d) NBs 3um

NB height with thickness 150nm has best reflectance below solar weighted reflectance 5%. But with increasing NB thickness up to 3um reflectance is significantly increased. We suspect that due to relatively small pitch (~10nm), these NB acts as a thin film without refractive index matching. This assumption reflects the red shift of reflectance peak shift. The reflectance peak is increased 350nm, 400nm 500nm with NB thickness 150nm, 1um, 3um.

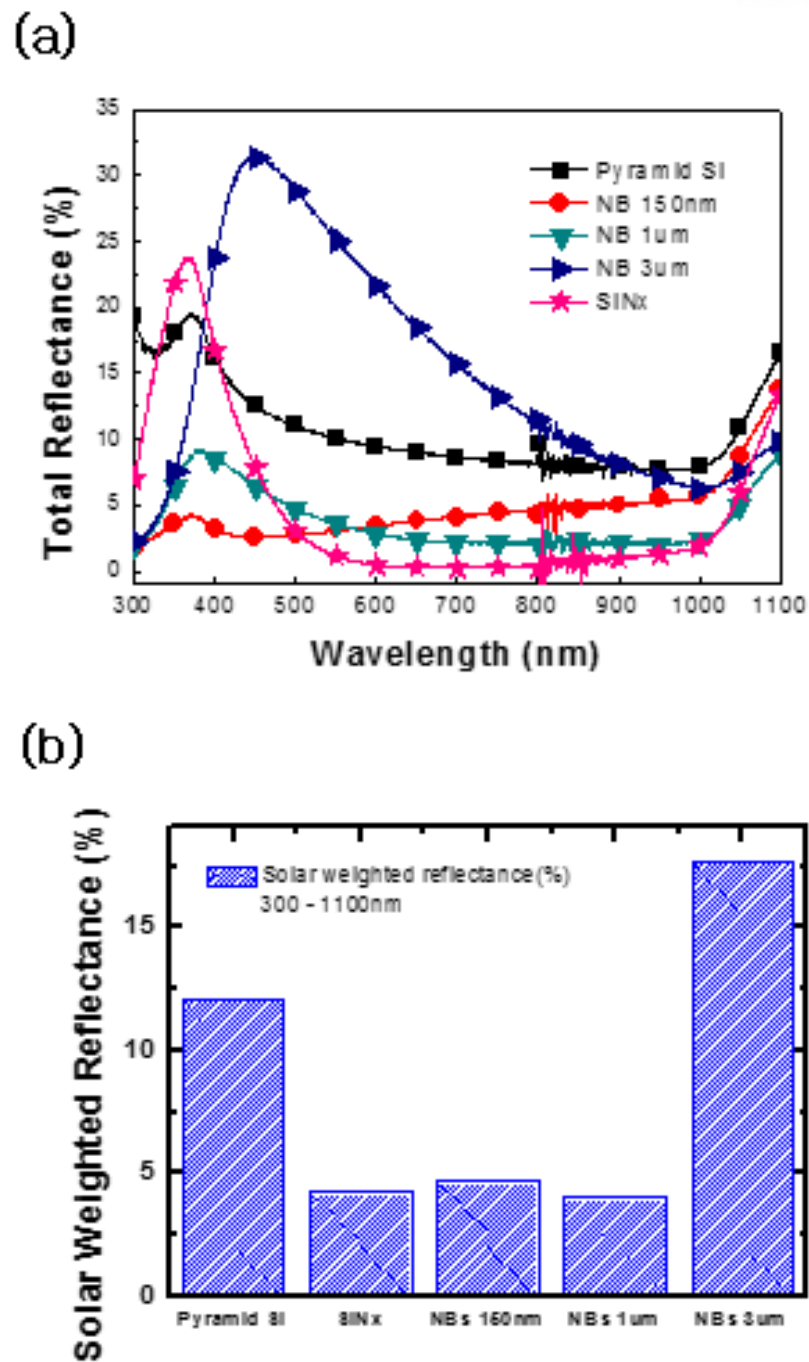
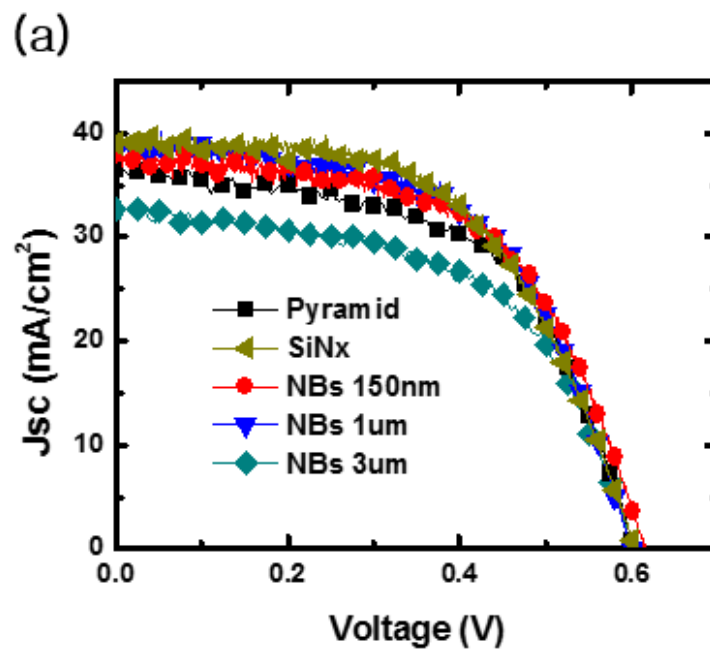


Fig 53. Total reflectance (a) and Solar weighted reflectance (b) with varying ITO nanobran-ches thickness on pyramid silicon



### 3.4.2.3 Electrical properties of textured silicon solar cell with Nanobranches

With combining textured silicon solar cell and nanobranches, significant efficiency enhancement is observed with increasing NB height.  $J_{sc}$  is increased almost 1.5mA for NBs 150nm. We cannot see any differences from  $V_{oc}$  and Fill Factor. This means that NBs affect only for compensating refractive index between air to textures silicon. These results are described in fig. 54



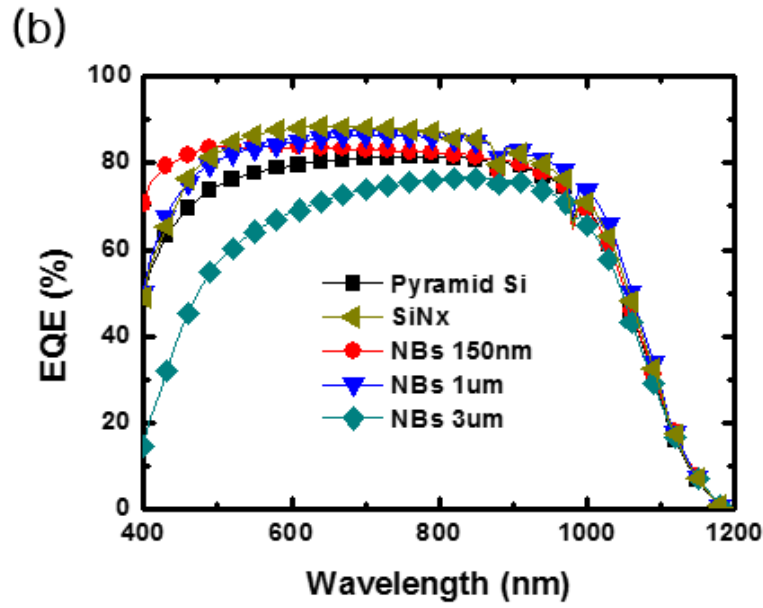


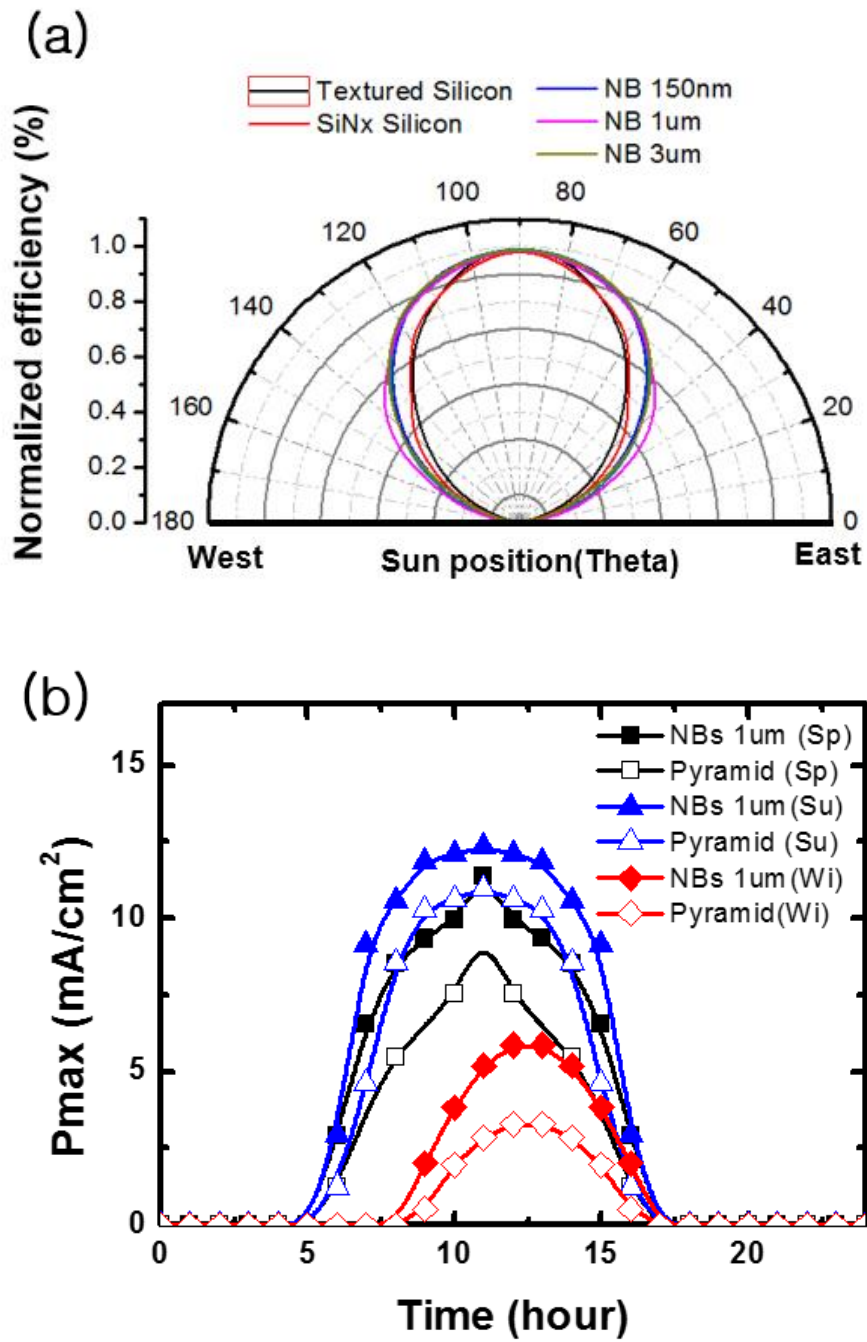
Fig 54. Textures silicon solar cell J-V characteristics (a) and EQE spectra (b)

	<b>J<sub>sc</sub></b> (mAcm <sup>-1</sup> )	<b>V<sub>oc</sub></b> (V)	<b>FF</b> (%)	<b>η</b> (%)
<b>Pyramid</b>	36.5	0.60	57.1	12.4
<b>SiNx coating</b>	38.7	0.61	57.0	13.2
<b>NB 150nm</b>	37.9	0.61	57.1	13.1
<b>NB 1um</b>	38.8	0.59	57.2	13.1
<b>NB 3um</b>	32.6	0.60	57.0	11.1

Table 3. Textured silicon solar cell parameters

To prove omnidirectional antireflection properties, we have measured solar cell efficiency with varying incident angles as described in fig. For textured surfaces, efficiencies is significantly decreased with increasing incident light because of Fresnel reflection. Compared to textured surfaces, SiNx single layer antireflection coating on textured silicon surface reveals more power densities at 30° but still single layer ARC doesn't compensate silicon's weak angular reflection. But our nanobranches reveals significant enhancement of angular properties for all incident angles. These omnidirectional properties significant increases daily integrated power density (measured at Seoul South Korea, Spring, Summer

Fall, Winter). Go forward, we calculated annual power densities for nanobranches 1um case which exhibits strongest omnidirectional characteristics. As a results nanobranch 3um generates more annual power densities about 44% compared to only textured silicon solar cells



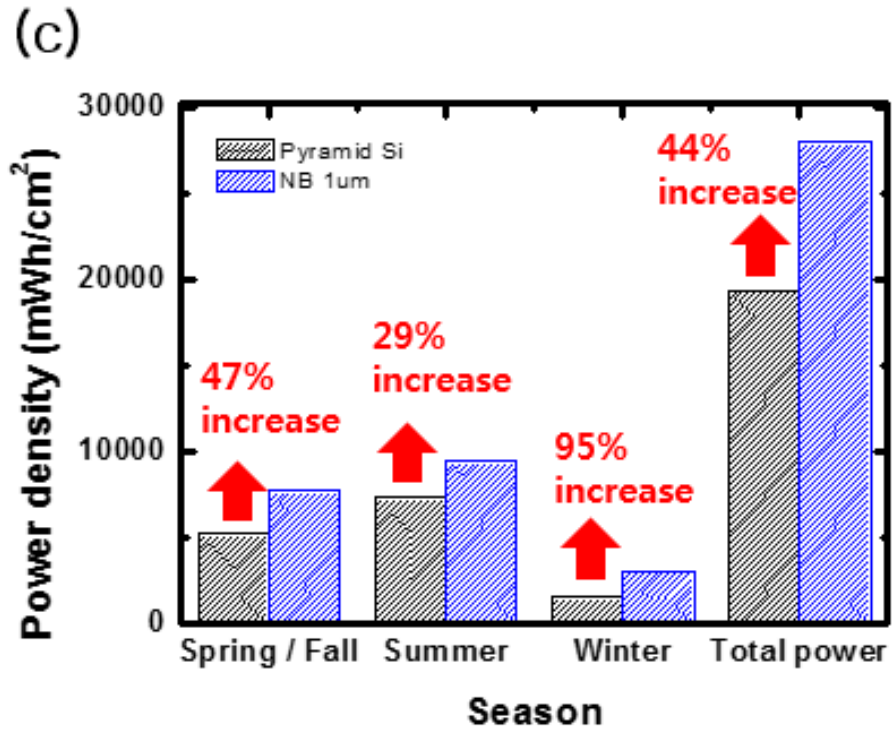


Fig 55. (a) Polar plot of normalized textured silicon solar cell efficiency with varying incident light, (b) Daily integrated power enhancement with Spring/Fall, Summer, Winter at Seoul, South Korea. (C) Annual power density of yramid and Nanobranches coated pyramid silicon solar cells

## Conclusions

In this study we have demonstrated Indium Tin Oxide (ITO) Fractal structures which has Graded Refractive Index (GRIN) profiles for Omni-directional Broadband anti-reflection coating to silicon solar cells. Indium Tin Oxide (ITO) Graded Refractive Index Fractal structures were deposited on silicon surfaces through self-catalyst vapor liquid solid growth mechanism using conventional Oblique Angle Deposition (OAD) with computational – controlled servo assisted electron beam evaporator while elevating substrate temperature below 200°C. We introduced two types of silicon solar cells. The first one has polished surfaces and second one has pyramids structure which is commonly used for industrial production. Graded Refractive Index (GRIN) Fractal structures were successfully applied to planar silicon surface and exhibits both superior optical and electrical properties. The total solar weighted reflectance is 7.8% while maintaining high transparency 96% at GRIN 2 $\mu$ m. Especially GRIN structure height 2 $\mu$ m on planar solar cell annual power density was increased 73.9% compared to w/o coating case due to reduced series resistance while maintaining shunt resistance and strong angular reflectance up to 70° below 10%. Furthermore for the conventional pyramid textured silicon which has self – induced oblique angle, Indium Tin Oxide (ITO) nanobranches were deposited onto pyramid without tilting servo. The deposited GRIN height 1 $\mu$ m exhibits superior angular response that can enhance its annual power density enhancement 44% compared to the textured silicon solar cell without any coating.

## References

- [1] S. Chattopadhyay, Y. F. Huang, Y. J. Jen, A. Ganguly, K. H. Chen, L. C. Chen, Anti-reflecting and photonic nanostructures, *Materials Science and Engineering: R: Reports*, vol. 69, pp. 1-35, 2010.
- [2] C. Lee, S. Y. Bae, S. Mobasser, H. Manohara, A Novel Silicon Nanotips Antireflection Surface for the Micro Sun Sensor, *Nano Letters*, vol. 5, pp. 2438-2442, 2005.
- [3] H. K. Raut, V. A. Ganesh, A. S. Nair, S. Ramakrishna, Anti-reflective coatings: A critical, indepth review, *Energy and Environmental Science*, vol. 4, pp. 3779-3804, 2011.
- [4] N. S. Wester, Image sensor with microlens material structure, US Patent US6577342, 2003.
- [5] H. F. MacMillan, H. C. Hamaker, N. R. Kaminar, M. S. Kuryla, M. L. Ristow, D. D. Liu, G. F. Virshup, J. M. Gee, 28% efficient GaAs concentrator solar cells, in: *Conference Record of the Twentieth IEEE, Photovoltaic Specialists Conference*, vol. 461, pp. 462-468, 1988.
- [6] N. Ph, R. Völkel, H. P. Herzig, M. Eisner, S. Haselbeck, Design, fabrication and testing of microlens arrays for sensors and microsystems, *Pure and Applied Optics*, vol. 6, pp. 617-636, 1997.
- [7] G. Agranov, V. Berezin, R. H. Tsai, Crosstalk and microlens study in a color CMOS image sensor, Electron Devices, *IEEE Transactions on Electron Devices*, vol. 50, pp. 4-11, 2003.
- [8] J. K. Holt, D. G. Goodwin, A. M. Gabor, F. Jiang, M. Stavola, H. A. Atwater, Hot-wire chemical vapor deposition of high hydrogen content silicon nitride for solar cell passivation and anti-reflection coating applications, *Thin Solid Films*, vol. 430, pp. 37-40, 2003. durable AR-coating, URL:<http://www.dsm.com/corporate/markets-products/markets/energy/khepricoat.html>, Accessed on 29th July 2014.
- [11] U. Schulz, Review of modern techniques to generate antireflective properties on thermoplastic polymers, *Applied Optics*, vol. 45, pp. 1608-1618, 2006.
- [12] J. M. Benyus, Biomimicry : innovation inspired by nature, Harper Perennial, New York, 2003.
- [13] P. Vukusic, J. R. Sambles, C. R. Lawrence, R. J. Wootton, Structural colour: Now you see it - now you don't, *Nature*, vol. 410, pp. 36-36, 2001.
- [14] A. R. Parker, H. E. Townley, Biomimetics of photonic nanostructures, *Nature Nanotechnology*, vol. 2, pp. 347-353, 2007.
- [15] K. -H. Jeong, J. Kim, L. P. Lee, Biologically Inspired Artificial Compound Eyes, *Science*, vol. 312, pp. 557-561, 2006.
- [16] R. Helbing, R. Gruhlke, Compact optical navigation module and microlens array therefore, US Patent US20070181785, 2007.

- [17] Image of a *Morpho Rhetenor* butterfly, URL: <http://www.medicaldaily.com/butterfly-settransform-nanotechnology-photonics-researchers-say-morpho-butterfly-wings-could-256160>, Accessed on 29th July 2014.
- M. R. Jorgensen, M. H. Bartl, Bioinspired Photonic Crystals: Diamond-Structured Titania Photonic-Bandgap Crystals from Biological Templates, *Advanced Materials*, vol. 22, pp. 107-110, 2010.
- [20] Corneal gratings reduce adhesion: Moth and Fly, URL: <http://www.asknature.org>, Accessed on 29th July 2014.
- [21] Eyes are antireflective: Elephant Hawk-moth, URL: <http://www.asknature.org>, Accessed on 29th July 2014.
- [22] A. Kelber, A. Balkenius, E. J. Warrant, Scotopic colour vision in nocturnal hawkmoths, *Nature*, vol. 419, pp. 922-925, 2002.
- [23] C. G. Bernhard, W. H. Miller, A corneal nipple pattern in insect compound eyes, *Acta Physiologica Scandinavica*, vol. 56, pp. 385-386, 1962.
- [24] C. G. Bernhard, W. H. Miller, A. R. Moller, The Insect Corneal Nipple Array. A Biological Broad-Band Impedance Transformer That Acts as an Antireflection Coating, *Acta Physiologica Scandinavica*, vol. 243, pp. 241-279, 1965.
- [25] Y. Su, B. Ji, Y. Huang, K. -C. Hwang, Nature's Design of Hierarchical Superhydrophobic Surfaces of a Water Strider for Low Adhesion and Low-Energy Dissipation, *Langmuir*, vol. 26, pp. 18926-18937, 2010.
- [26] X. Gao, X. Yan, X. Yao, L. Xu, K. Zhang, J. Zhang, B. Yang, L. Jiang, The Dry-Style Antifogging Properties of Mosquito Compound Eyes and Artificial Analogues Prepared by Soft Lithography, *Advanced Materials*, vol. 19, pp. 2213-2217, 2007.
- [27] J. Sun, B. Bhushan, J. Tong, Structural coloration in nature, *RSC Advances*, vol. 3, pp. 14862-14889, 2013.
- [28] L. Rayleigh, On Reflection of Vibrations at the Confines of two Media between which the Transition is Gradual, *Proceedings of the London Mathematical Society*, vol. s1-11, pp. 51-56, 1879.
- [29] M. J. Fraunhofer, *Joseph von Fraunhofer Gesammelte Schriften*, Munich, Germany, 1888.
- [30] L. Vaissie, O.V. Smolski, A. Mehta, E.G. Johnson, High efficiency surface-emitting laser with subwavelength antireflection structure, *Photonics Technology Letters, IEEE*, vol. 17, pp. 732-

734, 2005.

- [31] T. Okuno, Development of Subwavelength Structure Coating and its Application to Imaging Lenses, in: *International Optical Design Conference*, International Society for Optics and Photonics, pp. 765203-765203, 2010.
- [32] K. Sahoo, M.-K. Lin, E.-Y. Chang, Y.-Y. Lu, C.-C. Chen, J.-H. Huang, C.-W. Chang, Fabrication of Antireflective Sub-Wavelength Structures on Silicon Nitride Using Nano Cluster Mask for Solar Cell Application, *Nanoscale Research Letters*, vol. 4, pp. 680-683, 2009.
- [33] G. Bräuer, Large area glass coating, *Surface and Coatings Technology*, vol. 112, pp. 358-365, 1999.2000.
- [35] Y.-F. Huang, S. Chattopadhyay, Y.-J. Jen, C.-Y. Peng, T.-A. Liu, Y.-K. Hsu, C.-L. Pan, H.-C. Lo, C.-H. Hsu, Y.-H. Chang, C.-S. Lee, K.-H. Chen, L.-C. Chen, Improved broadband and quasi-omnidirectional anti-reflection properties with biomimetic silicon nanostructures, *Nature Nanotechnology*, vol. 2, pp. 770-774, 2007.
- [36] H. A. Macleod, Thin-film optical filters, 3rd Ed., Institute of Physics Publishing, Bristol, 2001.
- [37] G. A. Niklasson, C.G. Granqvist, O. Hunderi, Effective medium models for the optical properties of inhomogeneous materials, *Applied Optics*, vol. 20, pp. 26-30, 1981.
- [38] J. C. Maxwell-Garnett, Colours in metal glasses and in metallic films, *Philosophical Transactions of the Royal Society of London*, vol. 203, pp. 385-420, 1904.
- [39] J. C. Maxwell-Garnett, Colours in metal glasses, in metallic films, and in metallic solutions, *Philosophical Transactions of the Royal Society of London*, vol. 205, pp. 237-288, 1906.
- [40] D. A. G. Bruggeman, Berechnung verschiedener physikalischer Konstanten von heterogenen Substanzen. I. Dielektrizitätskonstanten und Leitfähigkeiten der Mischkörper aus isotropen Substanzen, *Annalen der Physik*, vol. 24, pp. 636-679, 1935.
- [41] M. G. Moharam, T. K. Gaylord, Rigorous coupled-wave analysis of planar-grating diffraction, *Journal of the Optical Society of America*, vol. 71, pp. 811-818, 1981. Arafune, Y. Ohshita, M. Yamaguchi, Y. Kanamori, H. Yugami, Antireflective subwavelength structures on crystalline Si fabricated using directly formed anodic porous alumina masks, *Applied Physics Letters*, vol. 88, 2006.
- [44] C. Seshan, Cell efficiency dependence on solar incidence angle, in: *Photovoltaic Specialists Conference*, Conference Record of the 35th IEEE, pp. 002102-002105, 2010.
- [45] X. Yan, D. J. Poxson, J. Cho, R. E. Welsch, A. K. Sood, J. K. Kim, E. F. Schubert, Enhanced Omnidirectional Photovoltaic Performance of Solar Cells Using Multiple-Discrete-Layer Tailored- and Low-Refractive Index Anti-Reflection Coatings, *Advanced Functional Materials*,



vol. 23, pp. 583-590, 2013.

[46] Laser and optical radiation, URL: <http://www.inchem.org/documents/ehc/ehc/ehc23.htm>, Accessed on 29th July 2014.

[47] Y. F. Makableh, R. Vasan, J. C. Sarker, A. I. Nusir, S. Seal, M. O. Manasreh, Enhancement of GaAs solar cell performance by using a ZnO sol-gel anti-reflection coating, *Solar Energy Materials and Solar Cells*, vol. 123, pp. 178-182, 2014.

[48] J. Thomas Cox, G. Hass, Antireflection coatings for optical and infrared optical materials, Physics of Thin Films Collection, Academic Press, New York, 1964.

[49] S.-Y. Lien, D.-S. Wu, W.-C. Yeh, J.-C. Liu, Tri-layer antireflection coatings (SiO<sub>2</sub>/SiO<sub>2</sub>-TiO<sub>2</sub>/TiO<sub>2</sub>) for silicon solar cells using a sol-gel technique, *Solar Energy Materials and Solar Cells*, vol. 90, pp. 2710-2719, 2006.

[50] R. Jacobsson, J. O. Mårtensson, Evaporated Inhomogeneous Thin Films, *Applied Optics*, vol. 5, pp. 29-34, 1966.

[51] B. Sheldon, J. S. Haggerty, A. G. Emslie, Exact computation of the reflectance of a surface layer of arbitrary refractive-index profile and an approximate solution of the inverse problem, *Journal of the Optical Society of America*, vol. 72, pp. 1049-1055, 1982.

[52] P. G. Verly, J. A. Dobrowolski, R. R. Willey, Fourier-transform method for the design of wideband antireflection coatings, *Applied Optics*, vol. 31, pp. 3836-3846, 1992.

[53] W. H. Southwell, Gradient-index antireflection coatings, *Optics Letters*, vol. 8, pp. 584-586, 1983.

[54] J. Q. Xi, M. F. Schubert, J. K. Kim, E. F. Schubert, M. Chen, S.-Y. Lin, W. Liu, J. A. Smart, Optical thin-film materials with low refractive index for broadband elimination of Fresnel reflection, *Nature Photonics*, vol. 1, pp. 176-179, 2007.

[55] B. E. Yoldas, Investigations of porous oxides as an antireflective coating for glass surfaces, *Applied Optics*, vol. 19, pp. 1425-1429, 1980.

[56] L.-Q. Liu, X.-L. Wang, M. Jing, S.-G. Zhang, G.-Y. Zhang, S.-X. Dou, G. Wang, Broadband and Omnidirectional, Nearly zero reflective Photovoltaic Glass, *Advanced Materials*, vol. 24, pp. 6318-6322, 2012.

[57] J. Noack, K. Scheurell, E. Kemnitz, P. Garcia-Juan, H. Rau, M. Lacroix, J. Eicher, B. Lintner, T. Sontheimer, T. Hofmann, J. Hegmann, R. Jahn, P. Lobmann, MgF<sub>2</sub> antireflective coatings by sol-gel processing: film preparation and thermal densification, *Journal of Materials Chemistry*, vol. 22, pp. 18535-18541, 2012.

